Innovations in Axial Flux Permanent Magnet Motor Thermal Management for High Power Density Applications

Colleen Jenkins, *Student Member, IEEE*, Samantha Jones-Jackson, *Graduate Student Member, IEEE*, Islam Zaher, *Student Member, IEEE*, Giorgio Pietrini, *Member, IEEE*, Romina Rodriguez, *Member, IEEE*, James Cotton, *Senior Member, IEEE*, and Ali Emadi, *Fellow, IEEE*

***Abstract*— For aerospace applications, power density is a major driving force in the design of electrified powertrains. At the forefront is the challenging design of electric motors with high efficiencies, torque, and power capabilities. Due to its high performance, the axial flux permanent magnet (AFPM) motor is expected to be one of the leading technologies to meet the demands of these industries. Finding the balance between the cooling system's effectiveness and subsequent parasitic losses is key to utilizing these performance benefits. Single-stator double-rotor topologies achieve the best torque density and lower stator losses and, however, are more challenging to cool as the stator is in the center of the motor. Single-stator single-rotor and double-stator machines are less challenging to cool but typically have lower power density. Rotor air cooling is discussed, including the effectiveness of blades, meshes, and vents, which can be optimized to prevent demagnetization. Stator cooling is critical as many machines maximize current density, producing a large amount of heat. The chosen strategy depends on the machine topology and can be accomplished by several strategies, including jackets, fins, channels, immersion cooling, hollow coils, and heat pipes.**

***Index Terms*— Axial flux permanent magnet (AFPM) synchronous motor, high power density, motor cooling, thermal management.**

I. Introduction

THE transportation sector is undergoing intense electrification to decrease greenhouse gas emissions (GHGs). There have already been significant advancements in passenger vehicles. Electric car sales increased 41% in 2020, and the global electric car stock reached the ten million units milestone [1]. However, improvements for heavy- and light-duty trucks have lagged in comparison. For example, global heavy-duty electric truck stock in 2020 was just 31 000 [1]. Recently, some of the key players in the heavy-duty truck manufacturing industry (e.g., Freightliner, Meritor, Kenworth, and Tesla) have started to propose electric powertrains based on motors with power ratings ranging from 200 up to 450 kW [2], [3], [4]. Heavy-duty trucks consume high amounts of energy, require batteries for long-range driving, and require high torque for hauling heavy loads. Electric motors must have high power density, efficiency, and torque capabilities [5]. Typically, an electric motor's torque target for long-haul heavy-duty trucks is 1000 Nm [6], [7], [8]. These ambitious specifications would not be possible without a reliable cooling system to control the temperature of the electrical machine.

The more-electric aircraft and all-electric aircraft (MEA and AEA) are other transportation fields with challenging powertrain requirements. Aerospace applications inherently need high power-to-weight ratios, thus occasionally pushing the continuous operating mode close to the overload limit of the machine. For example, the Evolito d1500/1 × 3 and d1500/2 × 3 have, respectively, 135 and 270 kW of continuous power but just 140 and 280 kW (+3.7% compared to the continuous mode) of peak power [9]. The automotive overload time is typically short (20–30 s), and the difference between the nominal and the overload power ratings is significant compared to aerospace applications. Consequently, the cooling system must reach a thermal steady state at load levels much higher than the automotive sector.

Among the most widespread technological trends in electric Vertical Take-Off and Landing (eVTOL) vehicle design is direct-drive propulsion, which removes the bulky transmission components between motor and propeller, thus enabling highly distributed propulsion systems [10]. As no gearbox connects the electric motor to the propeller, the aerospace industry's torque requirements are increasingly demanding.

The automotive and aerospace industry's primary concerns are reliability and safety. The wide range of operating scenarios due to the altitude creates challenging design constraints for aerospace cooling systems. A robust thermal management system is crucial to increasing motor performance and lifetime. Increased temperatures can lead to the permanent magnet (PM) demagnetization, material failure, and bearing lubrication deterioration, increasing losses in the machine [11]. Emerging high-power, high-torque devices require innovative thermal management solutions that can perform in numerous operating conditions and under tight packaging constraints with a minimal performance impact.

Manuscript received 30 September 2022; revised 21 December 2022; accepted 20 January 2023. Date of publication 8 February 2023; date of current version 13 September 2023. *(Corresponding author: Colleen Jenkins.)*

The authors are with the McMaster Automotive Resource Centre, McMaster University, Hamilton, ON L8P 0A6, Canada (e-mail: colleenmjenkins@gmail.com; jonesjas@mcmaster.ca; zaheri@mcmaster.ca; pietring@mcmaster.ca; rominarodriguez88@gmail.com; cottonjs@mcmaster.ca; emadi@mcmaster.ca).

Digital Object Identifier 10.1109/TTE.2023.3242698

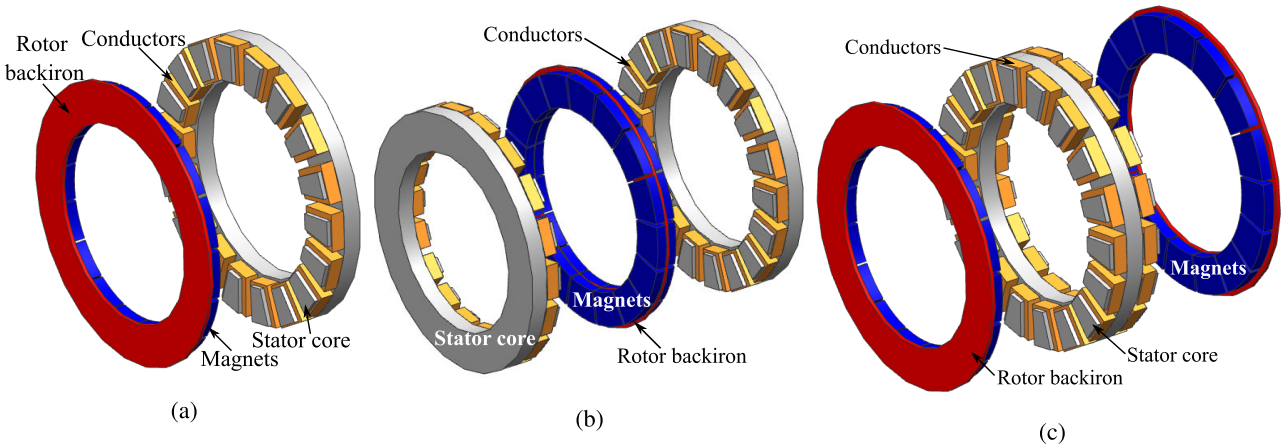

Fig. 1. Three main categories of axial-flux PM machines topologies [19], [23], [24], [25], [26], [27], [28]. (a) SSSR. (b) DSSR. (c) SSDR.

One of the most promising electric motor technologies for the two transport electrification applications mentioned above is the axial flux PM (AFPM) motor. An AFPM motor can achieve high torque and high power densities [19], [20], [21]. AFPM motors market is expected to reach $353 million by 2026 at a compound annual growth rate of 10.6% between 2021 and 2026 [22]. E-mobility, MEA, AEA, and eVTOL are among the main drivers of this growth. Table I reports some of the highest performance AFPM motors currently available. It can be observed that most AFPM motor manufacturers already have machines in their catalog compatible with the requirements for buses and heavy-duty trucks. Besides, some AFSPM companies specifically focus on aerospace electrification, such as Evolito, and others have special classes of motors for this industrial sector (e.g., AFE Eagle series).

This article will first discuss axial flux machine topologies in Section II and the primary sources of losses in the machine in Section III. Then, it will investigate the thermal management of two main sections of a PM axial flux motor: the magnets in Section IV and coils in Section V. Finally, materials and coolants related to the thermal designs will be discussed in Section VI. Future trends and innovations will be discussed in Section VII and concluded in Section VIII.

II. Axial Flux Machine Topologies

The axial flux motor architecture can be configured in multiple topologies [19], [23], [24], [25], [26], [27], [28], as shown in Fig. 1. Based on the number and the position of rotors and stators, three main categories can be defined.

1) The single-sided configuration consists of just one rotor and one disk-shaped stator. It is also known as a single stator single rotor (SSSR).
2) In the double-sided axial flux internal rotor (AFIR) configuration, one rotor is sandwiched between two stators, so there is a double stator single rotor (DSSR).
3) In the double-sided axial flux internal stator (AFIS) configuration, one stator is placed between two rotors [single stator double rotor (SSDR)].

Thanks to the double active air gap, double-sided AFPM motors exhibit a superior torque capability compared to the single-sided configurations [19], [20], [21], [24]. The main difference between DSSR and SSDR AFPM motors is that, with the first, the rotor yoke can be removed, while the stator yoke can be removed in the second. In either case, the mass of the machine decreases, while the power density is enhanced.

A. Single Stator Single Rotor

This machine topology is conceptually simple and similar to conventional radial flux machines, as the magnetic circuit requires a yoke in both the stator and the rotor to be closed [26]. However, the disk shape makes the manufacturability of these yokes much more challenging compared to radial flux motors. Laminations must be arranged in a spiral or cylindrical way. Therefore, normal stamping or laser-cutting cannot be used to make the slots directly in the stator's lamination pack. Another option is EDM, but the manufacturing cost increases significantly. The stator can also be split into teeth (which can be laser-cut and glued) and a yoke (which could be made by employing roll slitting followed by mandrel wrapping of the steel sheet strips), but the assembly complexity rises. An exciting alternative for the stator and rotor's iron cores is soft magnetic composites (SMCs). The SMC material is designed to make magnetic cores with unusual geometries, and its specific eddy loss is relatively low [29]. Sadly, its magnetic performance is inferior to high-end SiFe and CoFe laminations, particularly regarding saturation level and relative magnetic permeability. SMC's mechanical properties are poor: it is a highly brittle material, and its tensile ultimate/yield stress is typically one order of magnitude lower than steel due to its compressed iron-powder nature.

Another disadvantage of the single-sided configuration is the high axial force acting between the stator and the rotor [24], [25], [27], thus stressing the bearings, reducing their life, and increasing the friction loss. The main advantage of the SSSR topology is the cooling system. The stator yoke provides a large contact surface for the heat sink, and the laminations' thermal conductivity is high along the axial direction. However, due to the manufacturability issues described above and the lower performance, most of the AFPM motors on the market are not single-sided.

TABLE I

SUMMARY OF THE MAIN AFPM MOTORS AVAILABLE ON THE MARKET [9], [12], [13], [14], [15], [16], [17], [18]

Manufacturer	Model	Peak Power (kW)	Peak torque (Nm)	Max Speed (RPM)	Mass (kg)	Power Density (kW/kg)	Cooling System
AFE motors	Cheetah Small	32.5	41.8	10000	3.5	9.3	Liquid
AFE motors	Cheetah Medium	130	185	8000	16	8.1	Liquid
AFE motors	Cheetah Large	280	520	6500	28	10	Liquid
AFE motors	Cheetah Extra Large *	430	1020	5000	47	9.1	Liquid
AFE motors	Eagle Small †	21	41.8	5000	3.5	6	Liquid
AFE motors	Eagle Medium †	77.5	185	4000	16	4.8	Liquid
AFE motors	Eagle Large †	180	500	3500	28	6.4	Liquid
AFE motors	Eagle Extra Large †	290	930	3000	47	6.2	Liquid
AFE motors	Sailfish Small	32.5	41.8	10000	3.5	9.3	Liquid
AFE motors	Sailfish Medium	130	185	8000	16	8.1	Liquid
AFE motors	Sailfish Large	280	520	6500	28	10	Liquid
AFE motors	Sailfish Extra Large	430	1020	5000	47	9.1	Liquid
AVID	EVO AF125	100	220	12000	22	4.5	WEG
AVID	EVO AF130	140	350	8000	30.5	4.6	WEG
AVID	EVO AF140	220	600	5000	42.5	5.2	WEG
AVID	EVO AF230	280	700	8000	57.5	4.9	WEG
AVID	EVO AF240 *	440	1200	5000	82	5.4	WEG
AVID	EVO AF340 *	660	1800	5000	122	5.4	WEG
Emrax	188	60	90	6000	6.8	8.8	Air/WEG
Emrax	208	75	140	6000	9.1	8.2	Air/WEG
Emrax	228	100	230	5500	12	8.3	Air/WEG
Emrax	268	230	500	4500	19.9	11.6	Air/WEG
Emrax	348 *	300	1000	4000	39	7.7	Air/WEG
Evolito	d500 †	125	500	2500	20	6.25	Oil
Evolito	d1500/1x3 †	140	1350	2500	38.5	3.6	Oil
Evolito	d1500/2x3 †	280	1350	4000	38.5	7.2	Oil
MAGELEC	M19Px	145	131	15000	19.5	7.4	WEG
MAGELEC	M21Px	150	206	12000	23	6.5	WEG
MAGELEC	M21Sx	130	225	12500	23.5	5.5	WEG
MAGELEC	M21Rx	164	290	12500	23.7	6.9	WEG
MAGELEC	M24Px	201	368	9000	32.5	6.2	WEG
MAGELEC	M27Px	218	580	7350	43.5	5.0	WEG
MAGELEC	M34Px *	182	1114	4650	69.5	2.6	WEG
MagnaX	AXF185	100	100	12000	8	12.5	Oil
MagnaX	AXF225	170	250	10000	14	12.1	Oil
MagnaX	AXF275	300	500	8000	26.5	11.3	Oil
MagnaX	AXF350 *	480	1000	4000	42	11.4	Oil
Phi Power	Phi271	155	240	12000	20	7.8	WEG
Phi Power	Phi301	160	320	9000	29	5.5	WEG
Phi Power	Ph381	125	410	6000	38	3.3	WEG
Phi Power	Ph382 *	250	820	6000	68	3.7	WEG
YASA Ltd.	750R *	200	790	3250	37	5.4	Oil
YASA Ltd.	P400R	160	370	8000	28.2	5.7	Oil

* Good candidates for heavy-duty trucks, buses, etc.

† Motors specifically designed for aircraft applications.

B. Double Stator Single Rotor

The AFIR configuration typically requires less PM material because it only has one rotor. However, the PM mass savings is offset by more copper since the end windings are longer than the SSDR topology, as they must cross the motor axially to connect the coils in the adjacent stator [19]. Longer windings result in higher phase resistance and increased copper loss. Moreover, the machine construction issues described for the single-sided stator yoke also apply to the DSSR stators. Finally, air-cooling the rotor is challenging since the two sides are magnetically active and face a stator that can transfer its heat through a thin air gap.

Because of these disadvantages, the DSSR configuration is not the most widespread in the market although some manufacturers, such as MAGELEC Ltd. and Phi-Power AG, have selected this machine topology [15], [17].

C. Single Stator Dual Rotor

As mentioned above, the SSDR configuration needs less copper but more PM than DSSR [19]. However, thermal management of the magnets is easier; since the outside of the two rotors plays no magnetic role, it can be used for rotor air-cooling by adding effectively designed fins, as explained in Section IV. The two external rotors are exposed; therefore, two covers are required and must be designed to allow adequate airflow.

The SSDR configuration reduces the overall losses by, in some cases, utilizing shorter end-windings and removing the stator yoke [24], [25]. As the AFPM motor is a synchronous machine, the fundamental component of the magnetic field spins synchronously with the rotor, thus representing a constant magnetic flux in the rotor's reference frame. Therefore, the rotor's yoke loss is much smaller than the stator's (although not negligible, as will be discussed later).

Due to several advantages (see Table II), the SSDR topology is probably the most studied, so there are multiple configurations belonging to this category. The torus stator represents a well-known example, which can be either slotless or slotted [30]. In the slotless torus, the windings are wound around an iron ring [24]. This way, however, the windings are highly exposed to the rotor's magnetic field; hence, the ac copper loss reaches very high levels. Furthermore, the air gap must be expanded to accommodate the coils' thickness, lowering the electromagnetic performance. The problem is addressed by the slotted version of the torus SSDR [24], which consists of two "types" based on the PM magnetic polarization: the NN-type, where the poles of the two rotors are aligned, and the NS-type, where the rotors are shifted by 180 electrical degrees [31]. A problematic peculiarity of every torus with the stator yoke is the extra mass and manufacturing issues (strip wound electrical steel or SMC are the main options). However, the NS-type technically does not utilize the yoke for the equivalent magnetic circuit [32].

The yokeless and segmented armature (YASA) topology is the AFIS configuration with the most market penetration. Structurally, the main difference between a YASA machine and a torus is that a YASA is segmented, meaning that the stator is formed by distinct bar-shaped teeth [24], [25]. There is no stator yoke, and in the case of fractional slot concentrated winding (FSCW), each of the teeth can be wrapped in a single coil and eventually welded together in the desired winding scheme. This specific NS-type slotted stator is easily built compared to the other AFPM machines because it uses electric steel laminations cylindrically arranged. Furthermore, YASA motors outperform the other AFPM motor configurations in terms of torque and power densities, weight, and iron loss [25].

The possibilities of the axial flux topology have not been completely explored yet, and new interesting machine architectures are proposed in the literature [33] every day. Most of them, however, are small power prototypes, and their true industrial potential is still to be proven. As the main focus of this article is the thermal management and not the electromagnetic design of the AFPMs, we will consider only the main categories that have found industrial applications, especially in electric transportation.

III. Main Loss Sources

Even if this type of machine shows good maximum efficiency, the high power density achievable by these motors makes the rotor and stator cooling systems challenging. Due to the small volume and the machine construction, AFPM machine thermal limits often restrict overall performance. A tradeoff between structural and thermal properties typically drives the material selection to suboptimal cooling solutions.

This section examines the three dominant electromagnetic loss sources of the AFPM motors, with special regard to the YASA topology: PMs' eddy loss, winding's copper loss, and iron core loss [21]. As previously explained, the stator iron core of the YASA topology is substantially reduced compared to equivalent radial flux machines, so the iron core loss is usually less concerning.

A. Permanent Magnets

The AFPMs are synchronous machines, so the fundamental term of the rotating magnetic field spins at the same speed as the rotor. This property minimizes the rotor losses compared to asynchronous motors, as the magnetic flux density B into the rotor is almost time constant.

However, the magnetic field at the air gap is not a perfectly sinusoidal spectrum and contains spatial harmonics (such as those related to the stator slotting effect [34]) and sometimes subharmonics. These spectral components are not synchronous to the rotor spinning and, therefore, excite nonnegligible losses in the rotor. YASA motors often adopt FSCW arrangements, characterized by subharmonics with significant amplitude [35].

Both hysteresis and eddy losses are a function of the amplitude and frequency of B. While the frequency of subharmonics is lower than the fundamental, in AFPM motors, it should not be neglected. Thanks to their disk shape, YASA machines are suitable for rotor configurations with a high number of poles, thus maximizing the torque and power performance [36]. For instance, all the Emrax AFPM motors examined here have 20 poles [14]. On the other hand, the high number

TABLE II
COMPARISON OF THE AFPM TOPOLOGIES

Topology	Torque & power density	Permanent magnet mass	Manufacturing complexity	Electromagnetic losses	Cooling complexity
SSSR	-	-	+	+	-
DSSR	+	+	++	++	+
SSDR (YASA)	++	++	-	-	++

of poles increases all the electric frequencies of the motor, subharmonics included.

Consequently, the rotor losses, with special regard to the PM eddy losses, reach critical levels, and careful attention must be paid to the rotor cooling. Furthermore, in AFPM motors, the PMs are completely exposed to every air gap flux line. The relatively low resistivity of the sintered NdFeB magnets results in high eddy currents, unless proper countermeasures (e.g., segmentation) are taken [37], [38], [39], [40]. However, segmentation entails increased manufacturing complexity, thus raising the production cost. In AFPMs, the rotors are always attached to some structural machine part, which provides torque transmission to the shaft and mechanical support in both axial and radial directions to the magnets. Therefore, the magnets, together with the rotors, need to fit into these rotor carriers. The higher the number of edges and faces, the tighter the mechanical tolerances. Segmentation increases not only the machining but also the assembly complexity. The segments of each magnetic pole should be packed as tight as possible, but this way the magnetic forces are maximum.

B. Copper Loss

The uneven current distribution in the electric machines' windings is mainly due to the time-varying magnetic flux leakage in the slots [8], [41]. The skin and the proximity effects caused by the slot flux leakage reduce the active cross section of the conductors in the slots, thus increasing the ac resistance and copper loss [42].

Due to the large effective air gap, the slot flux leakage in the SPMs can easily account for 50% or more of the machine's overall inductance [43], [44], [45], [46], [47], [48]. Consequently, the AFPM motors are typically affected by substantial ac copper loss. Furthermore, the electric frequency of the AFPM motors can reach significant values since the number of poles is preferably high [14], [19], [20], [21], [36].

Many top-performing electric machines utilize copper bar windings to maximize the slot's fill factor. High current densities are also used to improve torque and power density but compromise the windings' copper loss dc and ac copper losses. Litz wire is another possible solution to the extra ac copper loss [49], [50] although, due to the high cost, it is not used normally in large-scale production. Litz wire can also decrease the fill factor of the stator slots.

The copper loss represents the dominant part of the electromagnetic losses in AFPM motors [21]. Therefore, highly effective cooling systems are necessary for the windings to prevent failures of the electric insulation layer, stator bar lamination adhesive, and bearing lubrication breakdown due to high temperatures [51].

C. Iron Core Loss

The iron core losses in the electric machines are due to the BH curve hysteresis and the eddy currents. Both these two effects are a function of the electric frequency of the motor, and as discussed in Sections III-A and III-B, the fundamental frequency of the AFPMs is not low typically because of the high polarity [14], [19], [20], [21], [36]. The most common approach to limit the iron loss without sacrificing the iron core magnetic performance is by utilizing higher grade magnetic laminations, thinner, and with a higher amount of silicon or just switching to cobalt steel CoFe and SMC. The AFPM designer can use higher grade material as well, but choosing the YASA topology can also represent a game changer.

By getting rid of the stator yoke, not only the mass of the machine is reduced but also all the iron losses associated with that part are canceled. This concept applies even more to the DSSR since there are two stator yokes.

The YASA topology enables also the utilization of grain-oriented electrical steel (GOES) [52], [53], [54], which was originally developed for the transformers, and shows much lower iron-specific losses compared to the nonoriented lamination steel, especially in overload conditions. The GOES magnetic properties are anisotropic; therefore, it cannot be used normally in rotating electric machines, as the magnetic flux direction in the teeth is different from that in the yoke. On the contrary, the flux in the YASA stator bars (or teeth) is mainly along the axial direction, thus making possible the application of this material to the YASA machines [52], [53], [54].

The only danger from the iron loss standpoint for the YASA motors is related to manufacturing. Sometimes, machining is used to achieve particularly tight mechanical tolerances or to make the wedge shape of the stator bars. This nonideal practice can compromise the insulation between the laminations of the stack in areas where the magnetic flux density is high, thus increasing the eddy loss. However, most of the manufacturers just rely on laser-cutting or stamping of the laminations without postmachining for this type of motor.

IV. PERMANENT MAGNET THERMAL CONSIDERATIONS

One critical machine failure mode is the demagnetization of the PMs resulting in torque loss. The primary cause

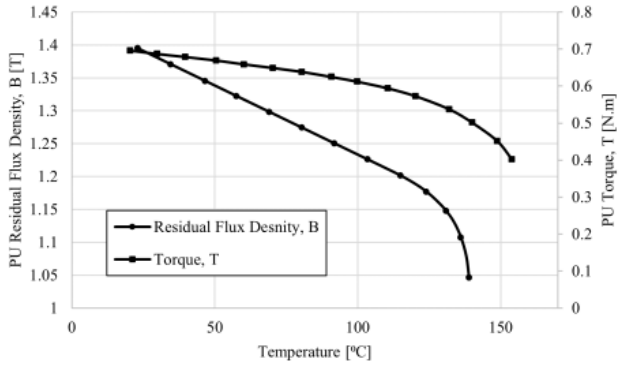

Fig. 2. Effect of magnet temperature on per unit residual flux density and per unit magnetic torque, from [55].

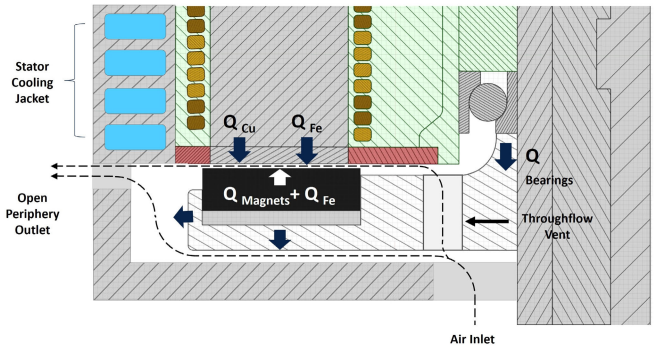

Fig. 3. Main losses and the cooling air paths for fully vented AFPM rotor.

of demagnetization is overheating. PMs undergo reversible demagnetization causing a reduction of their magnetic flux density as their temperatures rise. For neodymium magnets (NdFeB), commonly used in electric machines for the automotive industry, magnetic flux and magnetic torque reduce linearly as their temperature increases due to reversible demagnetization, as shown in Fig. 2. The reduction becomes more significant past 120 °C and reaches an irreversible demagnetization limit, and complete machine power loss is typically around 150 °C [55]. As an alternative to NdFeB, samarium cobalt (SmCo) magnets can be selected. Thanks to their higher Curie's temperature, SmCo magnets exhibit better magnetic performance at high temperatures. However, SmCo typically has a remanence flux density B_{rm} and a maximum energy product *BHmax* 25%–30% lower than NdFeB [56], so the SmCo performance at regular temperatures is worse compared to NdFeB, whereas SmCo price is usually higher than NdFeB. Due to this low benefit/cost ratio, SmCo is still a niche market material, while NdFeB represents the most prevalent PM option available in the industry.

Overheating the PMs in AFPM machines becomes a severe risk in high power density applications. Magnet eddy-current losses increase significantly due to higher excitation flux generation in the stator for higher magnetic torque within the often-limited cooling capacity of the rotor. Other thermal loss sources that contribute to the magnets overheating are the bearing mechanical losses, the rotor iron losses, and the windage heating losses. However, these losses can be significantly reduced by using low-friction bearings and non-electromagnetic rotor components. The impact of the windage heating losses on the magnets' temperature in AFPM machines is usually minimal due to their low-speed operation (<10 000 RPM). A representation of the losses and the cooling mechanisms affecting the PMs in an AFPM machine is shown in Fig. 3

A. Rotor Air Cooling

The rotor cooling capacity depends heavily on the cooling method, machine geometry, and operating speed. One advantage of the disk-shaped rotor of an AFPM machine is the inherently higher effective cooling surface area and relative air speed due to the larger machine diameter compared to its radial counterparts. Such an advantage makes air-cooling a favored cooling method, given the simplicity and lower parasitic power consumption of air-cooling systems compared to other types, such as two-phase and liquid cooling systems [57]. Despite the large body of literature body available on the topic of AFPM cooling, there is generally less emphasis on the topic of rotor cooling compared to stator cooling due to the lower losses in the former, especially in machines of relatively low power density. The AFPM rotor cooling is usually discussed in light of the more general topic of cooling of rotating disks due to the close resemblance to the rotor carriers. Rotor air cooling can be challenging due to the relatively low thermal properties (thermal conductivity, k, and specific heat capacity, C) of air as a coolant. Moreover, the cooling rate depends on the machine's operating speed and ambient conditions, causing further cooling system limitations. The cooling capacity can be improved by optimizing the rotor geometry to utilize the high relative air speed and turbulent flow patterns over the rotor and maximize the heat transfer rate over its surfaces.

1) Air Flow Over Rotating Disks: The rotor of an AFPM motor is commonly designed as a flat disk with surface-mounted or interior—buried-–PMs. The rotor disk is either enclosed between the stator and a cover in SSSR or SSDR machines, or sandwiched between two stators in a DSSR machine. Both topologies have a narrow axial clearance between the rotor surface and the stationary part of the machine, usually referred to as the air gap. The two opposing rotating and stationary disk surfaces in the air gap dominate the cooling system's effective heat transfer surface area, especially for an air-cooled rotor. Therefore, studying the flow over rotating disks is of great interest in understanding the associated flow patterns over the rotor surfaces and designing a suitable cooling system.

The flow patterns at the air gap are critical to the rotor heat transfer, with a direct influence on the magnet's cooling. The air film temperature and the average convective heat transfer over the magnets' surfaces are greatly affected by the type of air gap flow and net throughflow. The flow over the disk surfaces of the rotor can be classified into two main types according to the solutions originally introduced by Batchelor [58] and Stewartson [59], as shown in Fig. 4. In a Batchelor flow type, two boundary layers are formed on each disk surface, separated by a nonviscous rotating fluid

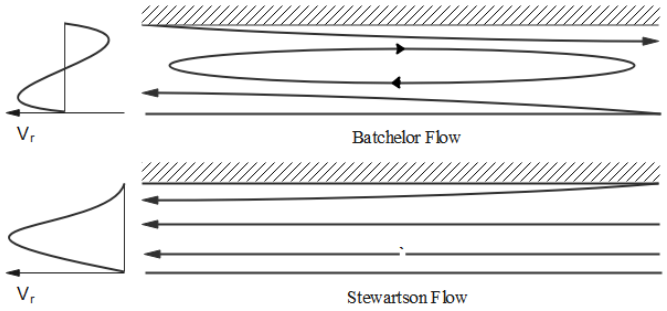

Fig. 4. Representation of the streamlines and the mean radial velocity profiles associated with Batchelor and Stewartson flow types in a typical disk rotor–stator system.

core. The boundary layers at the stator and rotor can be either turbulent or laminar depending on the rotor rotational speed and the resulting Reynolds number. Contrarily, the Stewartson flow type has no core rotation, and the tangential flow velocity across the air gap varies from zero at the stator boundary to a nonzero value near the rotor surface. Despite the contrariety of the two solutions, it was concluded through many studies that the Batchelor flow is mostly associated with enclosed rotor–stator assemblies [60], [61]. In contrast, the Stewartson flow type can be found in open periphery throughflow systems. Nevertheless, the Batchelor flow type can also exist in throughflow systems at a low Reynolds flow.

The studies in the literature showed that the air gap flow type is primarily a function of the rotor geometry and rotational speed. The air gap flow patterns and heat transfer in the reviewed studies are monitored and governed using the following parameters: the rotational Reynolds number, Re_θ, the nondimensional mass flow rate, C_ω, the Nusselt number, Nu, the air gap ratio ($G = s = R$), the flow entrainment coefficient, K (the ratio between the flow tangential velocity at the rotating core and the disk surface at the corresponding location), the local flow rate coefficient, Cq_r, and the Rossby number, Ro. The discussed variables can be expressed as follows:

$$\mathrm{Re}_\theta = \frac{\omega R^2}{\nu} \tag{1}$$

$$C_\omega = \frac{\dot{m}}{\mu R} \tag{2}$$

$$G = s/R \tag{3}$$

$$\mathrm{Nu} = \frac{hR}{k} \tag{4}$$

$$\mathrm{Cq}_r = \frac{Q_t \mathrm{Re}_{\theta,r}^{1/5}}{2\pi r^3 \omega} \tag{5}$$

$$\mathrm{Ro} = \frac{Q_t}{2\pi R^2 e \omega} \tag{6}$$

where ω is the rotor rotational speed in rad/s, R is the outer rotor radius, ν is the kinematic viscosity, $\dot{m}$ is the mass flow rate, s is the air gap thickness, h is the convective heat transfer coefficient, k is the thermal conductivity of air, Q_t is the volumetric flow rate, $\mathrm{Re}_{\theta,r}$ is the local rotational Reynolds number, and r is the radius.

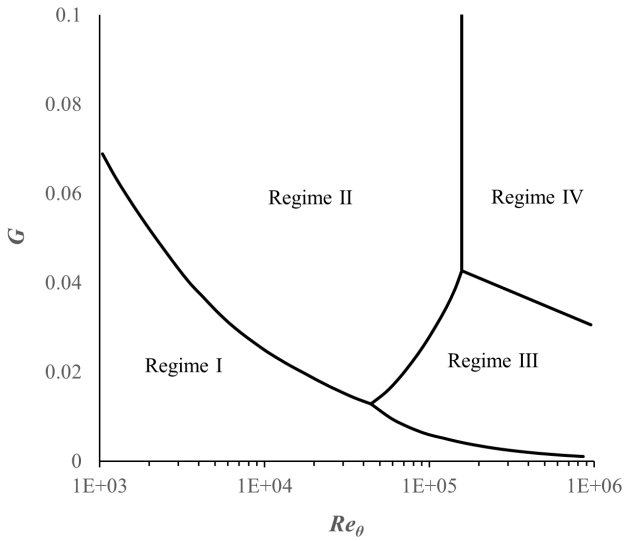

Fig. 5. Four air gap flow regimes as defined by Daily and Nece [62] based on G and Re_θ.

Daily and Nece [62] studied the flow in an enclosed rotor–stator assembly and classified the flow in the air gap into four different flows. They studied the different flow types by varying the rotational Reynolds number and the air gap ratio. Experiments were done using different air gap ratios at rotational Reynolds numbers ranging from 1E + 3 to 1E + 5. The authors proposed four possible flow regimes and related their existence to different combinations of the air gap thickness and the flow Reynolds number. The mentioned flow regimes can be classified into turbulent and laminar flows of merged or nonmerged boundary layers. According to Fig. 5, the following can be observed.

1) Laminar flow with merged boundary layers exists at low Reynolds numbers and small gap thicknesses.
2) Laminar flow with nonmerged boundary layers exists at larger air gap thicknesses, while, for a given air gap thickness, the laminar boundary layers can become unmerged at higher Reynolds numbers. For small gap thicknesses, the boundary layers will stay merged even at high Reynolds numbers before the transition into turbulent boundary layers.
3) Merged turbulent boundary layers exist at high Reynolds numbers and small gap thicknesses. At larger gap thicknesses, turbulent boundary layers may never become merged.
4) Nonmerged turbulent boundary layers can exist at any gap thickness if the Reynolds number is high enough.

It was also observed that a minimal radial outflow exists midplane across the air gap, and the average tangential velocity through the gap decreases as the gap thickness increases at a constant Reynolds number. Poncet et al. [63] investigated the turbulent flow in a rotor–stator system with and without a throughflow. The flow was studied experimentally and numerically at three different Reynolds number values and two different gap aspect ratios. The study concluded that the flow remains of the Batchelor type for closed systems and

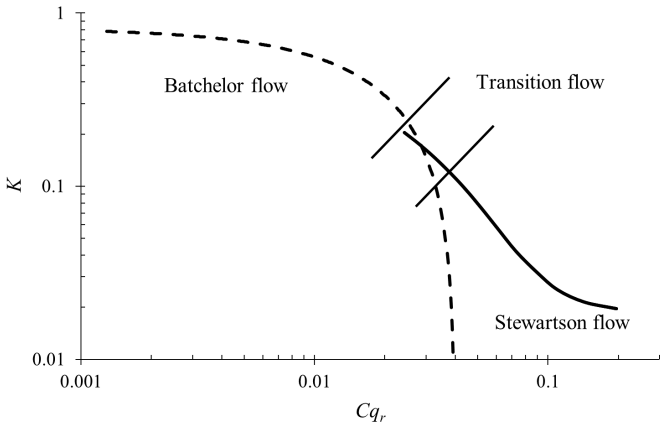

Fig. 6. Flow type dependence on local flow coefficient, Cq_r [63].

when a weak throughflow is allowed. The study also showed that increasing the Reynolds number at a given throughflow rate changes from Stewartson to Batchelor type. The results showed that both flow types can coexist at different disk radial locations, and the Stewartson flow tends to dominate the flow at the smaller radii.

The transition from Batchelor to Stewartson flow primarily depended on the throughflow rate. Two correlations that relate the flow entrainment coefficient, K, and the local flow rate coefficient, Cq_r, were derived from the collected experimental data shown in Fig. 6. Note that high K values denote the Batchelor flow type.

In a further study, Poncet et al. [64] studied the flow transition from the Batchelor type to the Stewartson type under the influence of superimposed throughflow. The results showed that the direction of the throughflow determines the flow type. Superimposed centripetal flow maintained Batchelor flow type, while it had faster core rotation than in the case of closed system Batchelor flow. The study also characterized the transition from Batchelor to Stewartson flow type using the Rossby number considering the radial position in the gap.

2) Heat Transfer in Rotating Disks: The different flow types discussed earlier are determinants of the heat transfer rate over the rotor surfaces. Many studies in the literature estimated and compared the heat transfer associated with the different flow patterns over rotating disks under different conditions. Cobb and Saunders [65] and Dorfman [66] studied the heat transfer over a heated free disk—without a stator wall—and derived correlations to estimate the Nusselt number for laminar and turbulent flows. The correlations provided by Cobb and Saunders and Dorfman are only applicable to a heated free disk. Accordingly, these correlations are insufficient to represent the heat transfer in an AFPM machine rotor, given the small clearances around its surfaces, especially at the air gap. However, the flow between the rotor and the shroud—or cover—can be of the free disk type if the air gap ratio is large enough. Owen and Rogers [67] defined a limit for gap ratio over which the stator influence on the air gap flow can be neglected, and the rotor can be assumed as a free disk. This limit is correlated with the rotational Reynolds number and can be calculated through the following equation:

$$G_{\text{lim}} = 1.05\text{Re}_\theta^{0.2}. \tag{7}$$

For any smaller gap ratio, the heat transfer at the air gap has to be analyzed based on the type of flow exhibited at the gap. In the case of fully enclosed shrouded rotor–stator systems, Owen and Rogers [67] analytically derived four mean Nusselt number correlations corresponding to each of the four flow regimes discussed by Daily and Nece [62].

Their results showed that, for low air gap ratios ($G < 0.01$) where the flow corresponds to either regime I (laminar) or III (turbulent) with a merged viscous boundary layer, the mean Nusselt number reduced as the gap ratio increased. At larger air gap ratios ($0.01 < G < 0.06$), where the flow exhibits regime II or IV, the mean Nusselt number is an increasing function of the air gap ratio. However, a rotating core between the two boundary layers reduces shear stress causing the mean Nusselt number to drop significantly compared to the smaller air gap ratio nearing that of the free disk.

Soo [68] analyzed laminar flow in a fully enclosed rotor–stator system with a superimposed inward/outward flow through an opening at the stator center. The study concluded that enforcing a net outward flow in the air gap is more beneficial for the rotor heat transfer compared to enforcing an inward flow. Poncet et al. [64] experimental study showed similar results and observed that the superimposed outward flow transitioned the flow from the Batchelor type to the Stewartson type. This transition results in better heat transfer over the rotor surface due to increased shear and lower average air gap bulk temperature.

Kapinos [69] and Owen [70] investigated the flow in an unshrouded rotor–stator system with a superimposed flow. The different flow types discussed earlier are determinants of heat transfer rate over the rotor surfaces, while this increase is dependent on the imposed mass flow rate, air gap ratio, and rotational speed. The study also concluded that the convective heat transfer is more dependent on the mass flow rate and less dependent on the rotational Reynolds number values at low Reynolds numbers for narrow air gaps ($G < 0.06$).

Boutarfa and Harmand [71] conducted a similar study. However, the rotor self-pumped the throughflow air without superimposing additional airflow from an external source. The results showed that the throughflow allowed through the stator opening increased the Nusselt number values on the rotor surface regardless of the Re_θ and G values compared to closed systems. The study was carried out for a range of rotational Reynolds numbers $5.87\text{E}+4 < \text{Re}_\theta < 1.4\text{E}+6$ at $G = 0.01$, 0.02, 0.06, and 0.17, as shown in Fig. 7. The comparison of flow in conjunction with the heat transfer at different gap ratios showed that, for smaller air gap ratios ($G \leq 0.01$), the Nusselt number over the rotor across the air gap is nearly constant. This agrees with Owen and Rogers, with a higher mean value than larger gap ratios at the same Re_θ. The author related the reduced mean Nusselt number in a higher gap ratio to the fact that they result in a lower air flow rate and Batchelor flow pattern across the air gap. They explained that, for $G = 0.01$, the air gap flow is dominated by the viscous forces resulting

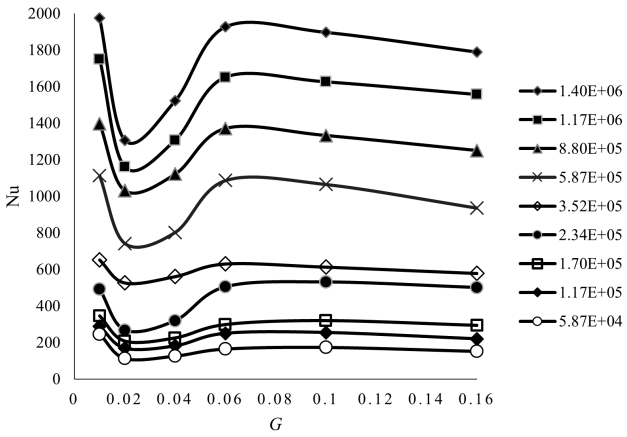

Fig. 7. Mean Nusselt number as a function of Re_θ and G [71].

in a Couette flow type filling the entire gap, similar to regimes I and III discussed by Daily and Nece. The result is a higher heat transfer rate at the inner radii, with relatively small boundary layer thickness. As the flow progresses to the gap periphery, the boundary layer thickness increases, and viscous forces become more significant, deteriorating the heat transfer. Moreover, the air temperature increases as it flows radially, reaching temperatures close to the rotor surface, which further deteriorates the heat transfer. Accordingly, the local heat transfer coefficient decreases proportionally with the radius. The results also showed that the heat transfer is enhanced significantly when the flow reaches the transition region.

Rasekh et al. [72] provided a comprehensive numerical study for the rotor heat transfer in AFPM machines. The study was carried out for an unshrouded rotor–stator assembly with axial openings in the rotor for throughflow ventilation. The rotor had surface-mounted magnet poles with annular air channels in between each pair, acting as a centrifugal fan and enhancing the system airflow, hence the heat transfer. The study varied multiple parameters, and correlations for the mean Nusselt number were derived accordingly. The correlation constants are optimized so that their results are not dependent on the system dimensions and ambient temperature. The results showed that, for values of $G < 0.01$, the heat transfer over the magnets on the rotor is directly proportional to the air gap ratio, in contrast to the results discussed by Owen and Rogers [67] and Boutarfa and Harmand [71] for air gap ratios larger than $G = 0.01$. The difference in results can be related to the much smaller air gap ratios tested in Rasekh's study. However, two other major differences that were not considered might have influenced the results. The first is the key difference between the studied rotor geometries. Second, the existence of annular air channels affects the flow field at the air gap as they become the primary air flow passage in the system according to the results presented by Howey et al. [73] and Airoldi et al. [74].

Howey et al. [75] reviewed previous air gap convection studies in axial and radial flux electrical machines. The authors concluded that, for small-sized machines to reach high power densities, introducing a superimposed flow at the air gap and increasing the roughness of the internal flow surfaces are recommended to increase the air gap heat transfer. This will maintain better flow turbulence and higher temperature gradients over the effective heat transfer surface area, hence higher cooling rates. However, the study by Nece and Daily [76] showed that surface roughness does not affect the frictional resistance on the rotating disk when the flow is laminar, while, for turbulent flows, increasing the disk surface roughness significantly increased the windage torque–the fluid frictional resistance torque—reaching nearly double the value of the smooth disk at high rotational speeds, given the direct relationship between the frictional moment and the average heat transfer over rotating disks [77]. It can be concluded that increasing the surface roughness of a disk operating at laminar flow speeds will not yield better heat transfer. In contrast, a significant enhancement in heat transfer can be yielded with turbulent flows but at the cost of increased frictional resistance. Therefore, this approach should be carefully studied concerning the machine operation speeds.

The discussed studies emphasize maintaining a small gap ratio ($G \leq 0.01$) and high rotational Reynolds number for better cooling of the magnets through the air gap in an AFPM machine. However, relying solely on the air gap to cool the magnets might not be enough. Hence, indirect cooling of the magnets through the rotor is usually necessary, especially for machines of higher power densities. Several studies have been performed to test the effect of different geometrical alterations on the improvement of rotor cooling.

B. Approaches for Rotor Air Cooling Enhancement

The low cooling rate of rotor air systems can be maximized under the same machine operating conditions by optimizing the rotor geometry to enhance turbulence, air mass flow rate, and, therefore, overall heat transfer. Many researchers have discussed this subject, and many approaches were proposed in the literature to improve rotor air cooling by enhancing its geometry, especially for SSDR machines. The following sections discuss the main approaches to improving rotor cooling in the literature.

1) Ventilated Rotors: Rasekh et al. [78] investigated the air flow in discoidal rotor–stator systems at a range of rotational Reynolds numbers $2.5\,\mathrm{E}+4 \leq \mathrm{Re}_\theta \leq 2.5\,\mathrm{E}+5$ and air gap ratios $G = 0.0067$, 0.0133, and 0.02667. The study results showed that vents/holes in the rotor body enable a net radial outflow through the air gap, hence increasing the air gap heat transfer effect. However, the study did not quantify or measure the claimed enhancement compared to a nonvented rotor. Airoldi et al. [74] also argued the benefit of having air admitted through the rotating rotor boss (hub) on the air gap heat transfer. The study focused on the heat transfer over only the stator side of the air gap, and the enhancement due to ventilation was also not quantified. Chong et al. [79] discussed the effect of rotor axial and radial holes in an air-cooled AFPM machine. The study showed a significant increase in the throughflow mass flow rate by introducing the holes, which enhanced the stator cooling result. Similar to Airoldi et al.'s study, the effect of the holes on rotor cooling was not assessed in this study.

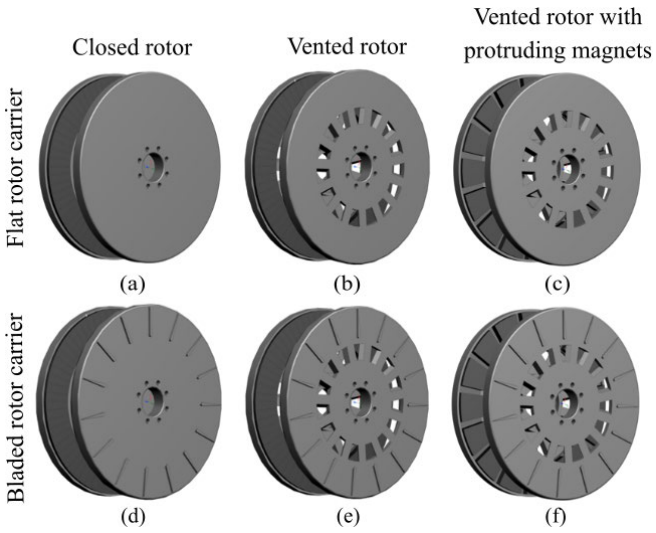

Fig. 8. Representation of the different rotor carrier geometries variations based on cooling features discussed in the literature. (a) Flat rotor carrier with a closed rotor. (b) Flat rotor carrier with a vented rotor. (c) Flat rotor carrier with a vented rotor and protruding magnets. (d) Bladed rotor carrier with a closed rotor. (e) Bladed rotor carrier with a vented rotor. (f) Bladed rotor carrier with a vented rotor and protruding magnets.

2) Surface-Mounted Protruding Magnets: The effect of surface-mounted protruding magnets on air cooling in AFPM machines was investigated by Airoldi et al. [74]. The thickness of the surface-mounted magnets and the rotational speed were varied in a validated computational fluid dynamics (CFD) model. The study found that increasing the height of the channels in between the magnets increased the pumping capacity of the rotor and the resulting windage losses. This effect resulted in enhanced heat transfer on the stator side of the air gap. Howey et al. [73] conducted a similar experimental study with two rotor configurations: one with a flat rotor surface, as shown in Fig. 8(a) and (e) and another with surface protruding magnets, as shown in Fig. 8(c) and (f). The study concluded that the average heat transfer over the stator side was increased by 20%–30% at similar operating conditions when surface protruding magnets were used. Rasekh et al. [72] studied rotor protrusions in AFPM numerically. Unlike the geometries presented in Airoldi et al. and Howey et al., the machine was throughflow ventilated through annular openings (channels) in the rotor. The geometry of the magnets, gap ratio, and rotational speed were varied in the study. The effect of each parameter on the heat transfer in the stator and the rotor was studied. The results showed that the overall heat transfer in the machine could improve substantially, especially on the magnets, by having both the rotor protrusions and the rotor openings simultaneously featured in the design. It can be argued that rotor protrusions are only effective in ventilated machines; hence, the author emphasized the equal importance of both features in the design for enhanced cooling.

3) Rotor-Embedded Radial Fan: In the efforts to maximize the rotor cooling in AFPM machines, Vansompel [80] suggested the addition of fan blades to the backside of the rotor to enhance the rotor heat transfer and structural rigidity. A well-known concept in the automotive industry for brake rotors cooling can only be applied to AFIS topologies. Fawzal et al. [81], [82] studied the implementation of this concept. Three fan geometries (backward-curved, radial/straight, and tear drop pillar blade) from other applications were investigated. Each geometry was modeled separately as an embedded fan section in an AFPM rotor. The performance of each fan design was judged based on the cooling capacity, pumping capacity, pressure drop, and windage losses. The study was done numerically using a validated CFD model of the machine. Although the study showed a significant enhancement in the rotor cooling performance with the addition of the rotor fan blades, this enhancement was not quantified. The results showed that the backward inclined had the best thermal performance among other geometries since it provides high cooling capacity at low additional windage losses. On the other hand, the radial blade offered slightly better cooling capacity but at the high cost of added windage losses. The authors introduced an index, the rotor cooling performance index (RCPI), to compare designs based on their convective cooling capacity and windage losses. Despite helping rank the designs based on two of the most crucial rotor design parameters, the index is calculated at equal temperatures of the rotor across all designs, hence, varying thermal load. Accordingly, the index comparison might not be directly applicable when comparing designs at constant thermal load.

In a further study, Fawzal et al. [11] studied the ventilation of the bladed rotor air cooling system and its effect on the machine's thermal performance. Three rotor shroud designs were studied with different variations of the location and shape of inlet and outlet ports. The first design had a radial inlet and radial outlet. The second design had a tangential inlet and tangential outlet. Finally, the third design had an axial inlet and tangential outlet. The three designs were modeled and simulated using CFD, where all simulations prescribed an equal mass flow rate at the inlet. The axial inlet-tangential outlet design resulted in the lowest pressure losses and significantly higher average heat transfer coefficient over the rotor at a comparable increase in windage loss values compared to the other designs resulting in an overall enhancement of the rotor thermal performance.

4) Rotor Liquid Cooling: Other motorized components in an electric vehicle can be integrated into the AFPM machine rotor to improve its cooling performance and power density accordingly. Nishanth et al. [83] studied the integration of a hydraulic radial piston pump with the rotor of a single stator AFPM. The design is optimized to maximize the pump leakage flow to improve the machine cooling capacity. The study showed a power density of 7.7 kW/kg at 12 500-RPM rated speed using conventional materials. Chuan et al. [84] proposed utilizing hollow shaft liquid cooling in conjunction with forced-in AFPM rotor. The study showed a significant improvement in the magnets' temperature by utilizing the hybrid cooling method over the air cooling method. The study compared the different cooling configurations using lumped parameter thermal network (LPTN) model. However, the hybrid cooling methods have to be further validated through detailed numerical and experimental studies.

Based on the discussed cooling features presented in the literature, different combinations of rotor cooling features can be used together to achieve higher air mass flow and cooling rate. This can be achieved in the same operating condition without significantly changing the machine design or dimensions. Zaher et al. [85] numerically studied and compared the thermal performance of six different rotor geometries, as shown in Fig. 8, considering different combinations of rotor cooling features (rotor vents, protruding magnets, and rotor fan blades). The different designs were ranked based on their cooling efficiency considering the maximum magnets temperature and the associated windage losses. The study concluded that having rotor vents that allow throughflow air is crucial for designing an efficient rotor air cooling system. Moreover, employing the rotor vents and the protruding magnets in the same rotor resulted in a significant reduction in the magnets' temperature at a marginal cost of added windage losses. Adding fan blades to the rotor resulted in a significantly higher mass flow rate, turbulence, and heat transfer over the rotor surfaces. However, the added windage loss (or the power consumed by the fan) might not be justifiable, unless a sufficient cooling rate could not be met using only direct cooling methods. This emphasizes the importance of maximizing the direct cooling of the magnets through either the air gap or air channels in between surface-mounted protruding magnets for efficient cooling of the rotor. Despite the drawbacks of using embedded fan blades for cooling the rotor, such systems can be optimized to maximize their cooling effect while maintaining the fan power moderately low. This can be done by optimizing the fan blade geometry using turbomachinery concepts, as discussed in [86].

V. Stator Winding Cooling Strategies

Stator cooling methods range widely from natural convection to two-phase liquid cooling, including forced air, outer liquid cooling jackets, flow channels, direct cooling, and heat pipes (HPs). The design of these cooling methods can significantly impact the machine's overall thermal, electrical, and mechanical performance. Since increased temperatures can reduce machine efficiency and cause adverse effects on motor stresses, the thermal management system must be selected such that it can effectively remove excess heat. Each cooling method comes with its benefits and drawbacks. Generally, natural and forced air-cooling for high power density motors is insufficient for stators in axial-flux motors. Sections V-A–V-F will focus on single- and two-phase liquid cooling. Liquid cooling in the literature is summarized in Table III, which displays the type of cooling method, the machine configuration, the coolant used, the machine power output, and the machine losses. When the machine losses are not readily available, the stator losses for the machine are substituted and marked with an asterisk.

A. Jackets

Stator cooling jackets are liquid cooling solutions that indirectly cool the copper coils since they are not in direct contact with the conductors. Generally, the coolant is in contact with the stator encapsulation or motor housing. A cooling jacket is either the sole stator cooling method or the manifold connection between different cooling channels. An outer jacket that contributes to the sole cooling function of the stator is one of the easiest and most common liquid cooling methods. While a wide range of design parameters can be altered depending on the design constraints, there are two common groups: the outer diameter (OD) cooling jackets and the end cover jackets. Typically, water, ethylene glycol (EG), and water EG (WEG) are used in these jackets (further discussed in Section VI-A).

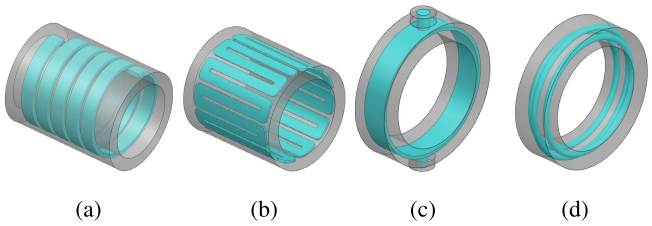

Fig. 9. Examples of OD liquid cooling jackets for axial-flux PM machines: (a) spiral cooling jacket [91], (b) axial channels [111], (c) single radial channel [88], [89], [90], and (d) parallel channels [87], [98].

Most commonly, stator cooling jackets for axial flux motors are located at the OD of the motor, as shown in Fig. 9, or at the end covers, as shown in Fig. 10. The size and cooling surface area of the jacket have a large effect on the heat transfer and, in turn, the stator temperature. Most commonly, the OD cooling jackets are used in the single-stator and double-rotor configurations, while end cover jackets are used in double-stator and single-rotor configurations. The goal is to ensure that the most heat can be removed from the stator, so the cooling location changes with the changing configuration.

Veg and Laksar [89] studied the impact of these two cooling systems with their respective configurations. In this study, the end cover cooling jacket was only required to cool a single stator (i.e., two end cover cooling jackets for the motor). It was found that the double-stator end cover cooling system had almost 30% lower total temperature than the single-stator OD jacket. This lower temperature is due to each system required to cool half of the losses the single-stator jacket dissipates. In addition, the end cover jacket allowed for greater temperature uniformity. However, this double-stator motor configuration requires more space than the single stator.

Furthermore, the greater surface area of the double-stator configuration allows for greater potential power output. This increased power is due to the greater cooling performance, which allows for greater power at the same temperature limitations. Although double-stator configurations are generally larger than single-stator configurations, the increased power output means similar power densities.

1) Outer Diameter Jackets: OD cooling jackets are limited in design due to the relatively low space availability. Commonly, these jackets are constructed from aluminum, but their flow path design ranges from spiral jackets [91], [111], axial flow paths [91], [111], parallel flow channels [87], [98], or a single channel [88], [89], [90], as shown in Fig. 9.

TABLE III
STATOR COOLING IN THE LITERATURE FOR AXIAL-FLUX PM MACHINES

Author/Year	Cooling Method	Machine Configuration	Coolant	Peak Power (kW)	Losses (kW)
Chuan *et al.* 2019 [84]	OD jacket	SSDR	Water	1.5†	0.177
Chang *et al.* 2021 [87]	OD jacket	SSDR	Water	50	–
Zhang *et al.* 2014 [88]	Single cavity/ OD jacket	SSDR	Water	65	4
Veg and Laksar 2019 [89]	Single cavity/ OD jacket	SSDR	Liquid	25†	1.67
Marcolini *et al.* 2019 [90]	Single cavity/ OD jacket	SSDR	Water	25†	3.2*
Le *et al.* 2020 [91]	OD spiral jacket	SSDR	Water	60†	3.14
Lampérth *et al.* 2015 [92]	Single cavity/ end cover jacket	DSSR	Water	79	–
Veg and Laksar 2019 [89]	Single cavity/ end cover jacket	DSSR	Liquid	25†	1.67
Odvářka *et al.* 2010 [93]	Inner core channel with spoilers	SSDR	Water	–	1*
Rahman *et al.* 2006 [94]	Single cavity/ OD jacket with fins	SSDR	Liquid	50	5.7
Qi *et al.* 2019 [95]	Spiral end cover channels	DSSR	Water	56	3.2
Liu *et al.* 2019 [96]	Cavity, spiral, tandem, and Z-shaped end cover channels	DSSR	Water	50	–
Lai *et al.* 2021 [97]	Z-shaped end cover jacket	DSSR	Water	100	3.03
Zhang *et al.* 2016 [98]	Copper pipe OD channels	SSDR	Water	70	8
Chang *et al.* 2021 [87]	OD jacket with winding channels	SSDR	WEG	65	–
Gerlando *et al.* 2020 [99]	Full-winding channels	SSDR	WEG	68†	6.8
Jones-Jackson *et al.* 2021 [100]	Full inter-winding / partial inter-winding	SSDR	WEG	–	4.4
Li *et al.* 2019 [101]	Serpentine inter-winding copper pipe	DSSR	Water	130†	8.44
Mohamed *et al.* 2021 [102]	OD jacket with fins	SSDR	Water	4	0.016*
Mohamed *et al.* 2022 [103]	Axial OD jacket with fins	SSDR	Water	–	2.08
Talebi *et al.* 2022 [52]	Microchannels on end windings	SSDR	WEG	250	14.37
Camilleri *et al.* 2012 [104]	Immersion cooling	SSDR	Liquid	100	6
Zhang *et al.* 2019 [105]	Immersion cooling with epoxy baffle plate	SSDR	Oil	53.8	2.2
Geng *et al.* 2020 [106]	Immersion cooling with baffles	SSDR	Oil	50	3
Wanjiku *et al.* 2021 [107]	Immersion cooling with baffles	SSDR	EG / Oil	50	15
Camilleri *et al.* 2016 [108]	Flooded stator with baffles	SSDR	Oil	100	6
Liu *et al.* 2021 [49]	Immersion with flow directing fins	SSDR	Oil	150	4
Lindh *et al.* 2016 [109]	Hollow copper coils	SSDR	Oil	100	3.4
Lindh *et al.* 2017 [50]	Hollow copper coils	DSSR	Oil	100	5.2
Le *et al.* 2021 [110]	Zigzag channels (series and parallel) with heat pipes	SSDR	Water	60	2.8

* Stator losses only

† Nominal/continuous power

Le et al. [91] compared two OD cooling jackets, one spiral channel, to an axial parallel flow channel jacket. They found that the spiral jacket impacted the rotor thermal performance and reduced the maximum rotor temperature by 3.4 K. However, they determined that the overall motor temperature still needed to be reduced, so they studied the effect of adding fins to the inner diameter of the cooling system. The fin results are presented in Section V-B.

Unlike the conventional OD cooling jacket design, Zhang et al. [98] swapped the single-channel jacket for five copper pipes in the stator. This water-cooling system is potted in epoxy to reduce the thermal resistance between the heat

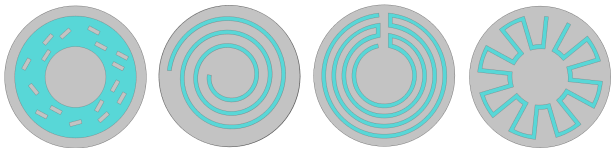

(a) (b) (c) (d)

Fig. 10. Examples of end cover cooling jackets for AFPM machines: (a) single channel or cavity [96], [115], (b) helical channels [96], (c) tandem channels [116], (d) z-shaped channels [95], [96], [114], and single fluid cavity [89], [92], [112], [113].

losses (generated in the stator segments and the windings) and the water-cooling system. While this study focused on mechanical analysis, the in-depth thermal performance analysis was out of scope. However, a computation fluid dynamics (CFD) analysis was done for the whole motor, primarily considering the airflow over the rotor. It was found that the PM temperature rises very quickly, and the air gap has a relatively low speed. Therefore, the rotor cooling was the limiting factor on speed and torque for this machine [98].

Furthermore, Tong et al. [111] studied the effect of the gap thickness between the stator core and the water jacket. A circumferential, or spiral, jacket design was used for a low-speed PM machine. The different gap thicknesses are considered based on different manufacturing tolerances. They found that the gap between the two materials linearly affects the maximum temperature rise. When the clearance is larger than 0.15 mm, the water-cooling system is likely no longer effective. The maximum temperature rise of the machine was greater than 80 K for this condition [111]. Since air has a much lower thermal conductivity than solid materials, epoxy is used in empty spaces to increase thermal performance.

2) End Cover Jacket: End cover jackets, compared to OD jackets, have more available space, and therefore, the flow path can range widely, as shown in Fig. 10. The most commonly found are the single fluid cavity [92], [96], [112], [113], helical [96], and tandem [95], [96], [114], [115]. In addition, Li et al. [96] studied the thermal performance of these types and a Z-shaped channel on a 50-kW motor. Also, their single-fluid cavity was equipped with spoilers to help direct the fluid flow and increase mixing. For each cooling system, the inlet and outlet diameters, and thermal conductivities were equal, neglecting the rotor impact.

Liu et al. [96] found that the Z-shaped channel had the greatest pressure drop, due to the sharp corners, with an inlet pressure of about 7.1 kPa. The cavity with spoilers was found to have the lowest pressure since the flow area was much larger. While this resulted in an inlet pressure of only 0.4 kPa, the fluid velocity in the cavity was much lower. The helical and tandem channels were found to have comparatively similar inlet pressures at about 1.8 and 2.8 kPa, respectively. In terms of the thermal performance, however, all channels, besides the cavity with spoilers, saw similar maximum fluid temperatures, around 81 °C–82 °C. Due to the low fluid velocity, the maximum temperature in the cavity was about 91 °C (using coolant at 25 °C and 30 °C for ambient).

Therefore, since the tandem channel saw the lowest maximum temperature, at 81 °C, Liu et al. studied the geometrical effects on thermal performance. They studied the impact of the number of channels, axial channel length, radial channel length, and inlet velocity. When the number of channels was studied, the cooling surface area stayed the same, but the channel width decreased with an increasing number of channels. It was found that the pressure drop increased, while the temperature decreased with increasing channels. To balance these two factors, they concluded that the optimum number of channels was 3–5. Furthermore, they found that the axial and radial length of the channels had a significant impact on the pressure drop but less on the temperatures. Using the tandem water-cooling channels, they selected the following parameters: five channels, 10 mm of axial length, 12 mm of radial length, and an inlet velocity 0f 0.8 m/s. This analysis showed a maximum motor temperature of 95 °C at the end windings [96].

Qi et al. [95] and Huang et al. [114] also studied a tandem cooling channel for their 36-kW machine, with a maximum power of 56 kW. This motor also used five cooling channels with a width of 10 mm. With an inlet flow rate of 12 LPM and an ambient temperature of 60 °C, the maximum winding temperature is 109 °C. However, after operating at maximum power for 1 min, the maximum winding temperature increased to 171 °C. They concluded that the insulation grade is rated at 200 °C, so there is still a safety margin [95], [114].

In addition, Chai et al. [112] and Bi et al. [113] studied the impact of the thermal resistance heat path on the machine temperatures using a single channel end cap for each of the two stators. Extending the end cap toward the end windings (removing the epoxy in its place) decreased the thermal resistance from the stator yoke and windings to the cooling system. Two principal factors were studied to determine the effects on the thermal performance: the epoxy thermal conductivity and the stator yoke thickness. The increase in epoxy thermal conductivity improved the average winding temperatures of both end cap designs. The extended end cap saw almost a 6 °C temperature reduction at the lowest epoxy thermal conductivity (0.4 W/m-K). However, this temperature difference was reduced with increasing epoxy thermal conductivity. A more considerable difference was seen with the changing stator yoke thickness. While the temperatures increased in both designs with thicker stator yokes, the extended end cap saw a 10 °C decrease in average winding temperature at the thickest yoke (25 mm) [113].

Furthermore, Bi et al. [113] studied both designs at an overload condition (700 Nm at 100 RPM) for 180 s. They concluded that the extended end cap design could keep the maximum machine temperature below the limit (130 °C) while 5.3 °C lower than the conventional design. The result was an additional 23 s, past the requirement for the modified end cap [113].

B. Heat Transfer Fins

The cooling performance of liquid jackets can also be improved with extended protrusions or fins. The addition can improve the thermal resistance from the heat-generating components by increasing the contact surface area of the cooled

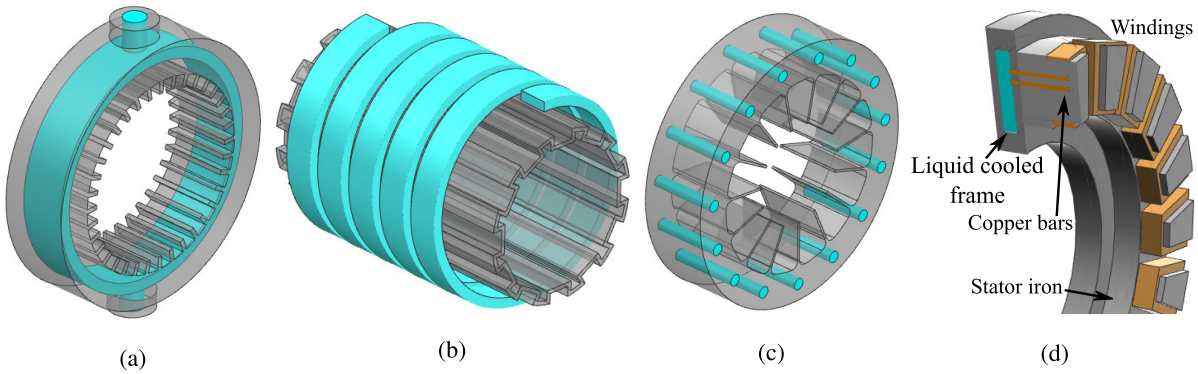

Fig. 11. Stator cooling fins: (a) connected to the cooling jacket at the OD of the stator [71], (b) at the inner diameter of the stator spiral jacket [89], (c) [98] and [105], and (d) copper rods extruding into the stator [106], [107].

jacket material. Le et al. [91] used a spiral OD water jacket combined with twelve rectangular fins protruding toward the windings on the inner diameter of the housing, as shown in Fig. 11(a). By varying the width and depth of these fins, an almost 15 °C reduction in maximum rotor temperature was seen compared to the spiral jacket alone, without fins. They found that the rotor temperature was stable (no longer decreasing) at a width and depth of 15 and 6 mm, respectively. The resulting maximum rotor temperature was 121 °C for the 60-kW machine.

Fins have been used in axial flux motors for long-term testing. Rahman et al. [94] designed a 25-kW AFPM with an aluminum liquid cooling ring to be placed in the OD of the machine stator. A schematic of a cooling ring with aluminum fins is below in Fig. 11(b). This cooling ring is equipped with fins between the winding turns and potted with a high thermal conductivity epoxy. The developed wheel motor and cooling system were patented, placed in a GM S10 mule vehicle, and driven over 1000 mi.

Mohamed et al. [103] and Vansompel et al. [117] have published some papers on their YASA AFPM machine designs. Each machine is cooled with a different coolant flow path and is adjusted whether the power converter is integrated with the machine. However, the stator heat-extracting fins have stayed the same between these designs and are shown in Fig. 11(c). The cooling design is made from a stack of 2-mm aluminum alloy sheets to make a stator housing with fins. This allows for a high thermal conductivity parallel to laminations and winding strands, and low in the perpendicular direction. In the nonintegrated motor, the cooling effect of the heat-extracting fins is analyzed by Vansompel et al. [117]. Here, a coolant is not specified, but a CFD model and a constant heat transfer coefficient (convective boundary condition of 40 W/m^2-K, with a reference temperature of 25 °C) are applied to the fins. While they found the fins increased the losses from 65 to 80 W, the motor temperature was much cooler. Due to the low thermal conductivity of the potting material, without the fins, there is a large temperature gradient over the epoxy. The introduction of these fins allowed for a much smaller temperature gradient within the stator [117].

On the other hand, Mohamed et al. [103] studied a similar aluminum fin structure with an integrated inverter module and axial flux machine. While the fins were the same design as in [117], a single cooling channel was added per module, with one inverter module per stator coil. Several design changes were studied, including swapping the aluminum housing for copper, a new thermal interface material (TIM) with an improved thermal conductivity (between the cooling and power modules), and three channels per module instead of one. Out of the three improvements, the TIM significantly impacted the increased power density (at the same temperature). The improved thermal conductivity increased the normalized power density by 52%. In addition, the copper housing increased the winding losses from 73 W, per module, to 83 W. This resulted in a hotspot of 115 °C or a reduction of 3 °C winding hotspot temperature compared to aluminum. This hotspot was seen with an inlet water temperature of 25 °C, 1 LPM flow rate, and 7.45 W in switching losses. Furthermore, combining all three improvements, the normalized power density increased by 91% [103].

Alternatively, Polikarpova et al. [118] and Pyrhonen et al. [119] have implemented copper bars extending from the liquid-cooled frame into the stator iron for the double-stator AFPM machine. An example with two copper bars shown is displayed in Fig. 11(d). Most of the winding heat was transferred through the stator iron toward the cooling system. The copper bars can extract the stator heat combined with the stator teeth. A total of three bars per tooth were selected, and it was stated that any more would cause mechanical stability problems. No significant losses are generated since these copper bars are parallel to the magnetic flux path. However, a slight increase in iron losses is seen due to the increased flux density (more current in a smaller area) but is deemed insignificant. They found that just a single copper bar in each stator tooth contributed to a reduction of 6 °C of the maximum stator slot winding and end winding temperatures compared to just the jacket. It also had a 10 °C reduction in the maximum rotor-embedded magnets. In addition to the copper bars, a potting material is included in the stator. They see further reductions in maximum temperatures with both thermal improvements included compared to just the jacket. It is found to have 21 °C, 21 °C, and 25 °C reductions in the slot windings, end windings, and magnets, respectively [118].

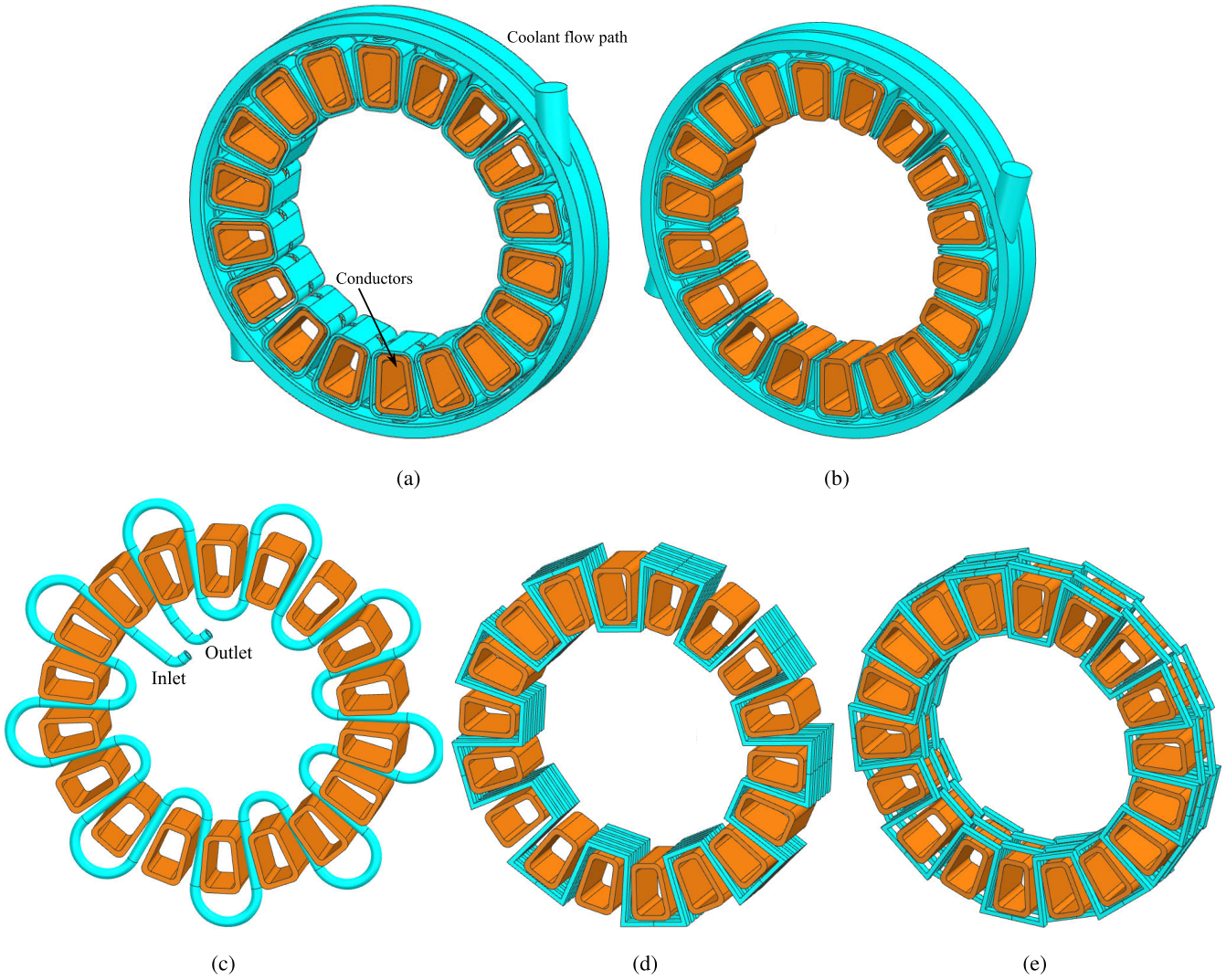

Fig. 12. Different channel cooling configurations for stator cooling: (a) full interwinding for indirect cooling, (b) full interwinding for direct cooling, (c) single copper pipe, (d) multiple copper pipes, and (e) alternating copper pipes.

C. Internal Flow Channels

Due to sizeable copper losses in the stator, the most effective cooling methods reduce the thermal resistance from the coolant to the windings. One popular cooling enhancement includes cooling channels that come as close to the coils as possible.

By reducing the thermal resistance from the cooling system to the heat-generating components, the output power can be increased, as well as other key performance metrics. Chang et al. [87] studied the motor performance improvement of a conventional water-cooling jacket by adding channels connected to the same jacket. These channels flowed in between adjacent windings. This analysis found that the peak power could be increased from 50 to 65 kW with the jacket and the introduction of the channels, respectively. It was found that the peak torque, rated power, and rated torque could be increased by 14.3%, 33.3%, and 9.1%, respectively [87].

Examples of different cooling channel designs are shown in Fig. 12. The configurations include full interwinding channels, for indirect and direct cooling, in Fig. 12(a) and (b), respectively. In addition, copper has been used to make channels or pipes that meander adjacent windings. This is done with a single copper pipe and several, as shown in Fig. 12(c)–(e). Also, cooling channels have been embedded in the stator core, as shown in [93].

By including channels in the stator cooling system, the cooling configurations expand. Most commonly, channels are connected to a manifold, similarly designed to the OD cooling jackets, especially when the coolant flows through each channel parallel to one another. However, channels can have an in-series coolant flow path, and a manifold is less common.

For parallel cooling channels connected by a manifold, most commonly, the channels wrap around the entire OD of the coils. These are described as full interwinding designs since they cover the full surface between the neighboring windings. However, there are also partial interwinding designs. By reducing the space of the cooling system, the machine design can become more compact [100]. Care must be made since reducing the cooling capacity can reduce the motor performance. To further decrease the thermal resistance between the coils and the coolant, these channels can be cooled with dielectric coolants, such as oil. Dielectric coolant can allow

the liquid to contact the copper windings directly. However, water-cooling channels must have an insulating buffer between the fluid and windings. Although water has a higher thermal conductivity than oil, this insulating layer can seriously reduce the cooling capacity [100].

Jones-Jackson et al. [100] studied the stator performance between a full interwinding design and two partial interwinding designs. The full interwinding cooling design had the lowest thermal resistance due to the high cooling surface area. When comparing two very similar designs, one as a partial interwinding design and one as a full interwinding design, the thermal resistance decreased by about 19% with the full coverage design [100].

Li et al. [101] took a different approach by using copper pipes to make two meandering parallel paths inserted into the slot at the stator tooth's bottom. The pipe has an OD of 16 mm and is clamped to a support structure that connects the stator tooth to the end cap. In addition, this support structure acts as a barrier between the copper pipe and the windings. The copper pipe was selected due to its high thermal properties, which allows for more effective heat dissipation. In the analysis, the copper windings are assumed to be solid bodies with a realistic winding thickness (instead of modeling each turn). The maximum coil temperature is seen in the end windings. Using an inlet temperature of 30 °C and 9.5 kW of losses in the motor, the maximum temperature rise is almost 60 °C, at a maximum end winding temperature of 89 °C. These results were also validated with the 130-kW prototype, showing a maximum end winding temperature of 90 °C [101].

Similarly, Le et al. [110] used five copper water pipes to direct flow in the stator between adjacent windings. They found that the placement of the inlet and outlet with respect to one another can impact the temperature distribution. Since an uneven temperature distribution in the motor can lead to an unbalanced three-phase resistance and degrade the electromagnetic performance, this cooling system is inadequate. However, by placing the inlet and outlet 180° from each other, the coolant temperature rise, and the stator temperature gradient is reduced. The offset inlet and outlet had the lowest pressure drop, 25 kPa, compared to 28.6 kPa in the neighboring inlet and outlet designs. Lowered pressure drop resulted in a 13% pump energy reduction compared to the other designs [110].

On the other hand, Odvářka et al. [93] created a cooling channel through the stator core. It is made from aluminum, sandwiched between two stator core halves, and contains fins to guide the flow. With flow at 10 LPM, 1000 W of stator losses, and an inlet temperature of 65 °C, they found only a 2.8 °C increase in coolant temperature from the inlet to the outlet.

D. Immersion Cooling

Direct cooling by immersion includes complete motor flooding, total stator flooding, or semiflooded concepts. Due to the high speeds of this application and increased rotor windage losses, fully flooded solutions are typically not chosen. In AFPM motors, total stator immersion cooling is the most common direct cooling method. Innovations in this design implement baffles, fins, flow reducers, heat sinks, and intricate coil designs to create an even flow distribution from inlet to outlet and maximize the contact area between the coils and coolant.

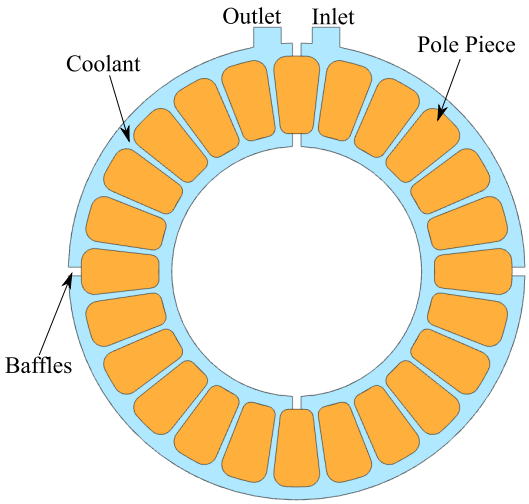

Fig. 13. YASA AFPM motor immersion baffle design [108].

Camilleri et al. [104] characterized the temperature distribution of the YASA-750 AFPM motor, which implements a flooded stator design and has a peak power of 100 kW and a peak efficiency of 94%. They created a test setup representing the motor's pole, winding, and flow passages. The passages, winding, and core were fit with 22 thermocouples, and the exterior of the setup was constructed to minimize heat loss to the ambient. Tests were conducted at a motor operating point of 1500 RPM and 300 Nm, equivalent to 50 kW in power. Flow rates between 4 and 10 LPM were tested, resulting in a laminar flow regime. Decreased flow rate showed more significant hot spots and poor temperature distribution. The highest temperature was measured at the inner mid-winding, away from the coolant and iron core. As the flow rate increases, the imbalance between the different flow paths increases, creating a high-temperature gradient in the stator.

Improving on the YASA Ltd. design, Camilleri et al. [108] demonstrated an immersion cooling design implementing baffles that divide the stator cavity into four sections creating an even flow distribution between the stator coils, as shown in Fig. 13. The design reduced hot spot temperature by 13 °C and increased current density by 7%. The inlet flow rate was 6 LPM, and the temperature was 80 °C. A quarter stator setup was created to test the design. A total of eight tests were completed at different flow rates, inlet temperatures, and heat losses, which verified simulation results within 6% of the measured temperature. The authors noted that this design could be enhanced by decreasing the width of the outer race and adding flow reducers in the inner and outer races to increase the head loss in the system [108]. Further improvements to the design are shown in [107], [120], and [121].

Camilleri and McCulloch [120] added a heat sink to the baffled design, which increased current density by 140% and

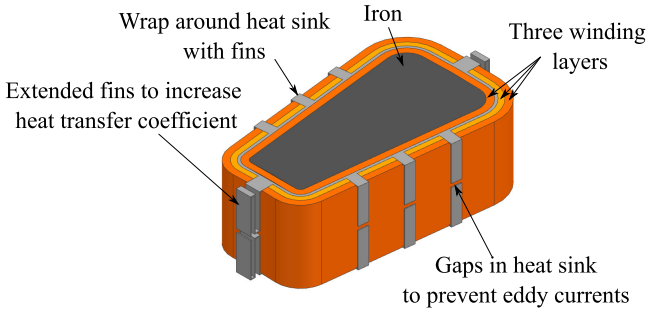

Fig. 14. YASA AFPM motor immersion heat sink design [120].

decreased hotspot temperature by 87 °C compared to the initial YASA Ltd. construction. The design used traditional concentrated winding AWG14 and the synthetic dielectric coolant Opticool. The heat sink is made of 0.1-mm sheet copper and is placed between the inner and middle windings extending out into the stator cavity, as shown in Fig. 14. The design removes heat from the inner mid-winding, the hot spot in previous designs [104], [108], and moves it to the iron core. A single coil thermal setup of a prototype heat sink was completed, and found models were within 3% of experimental results. The design offers a significantly reduced coil temperature, leading to increased winding life, reduced resistive losses, and increased current density at the maximum operating condition. While this design shows significant improvement in thermal management compared to the baffle design, the electromagnetic effects and eddy current losses were not assessed with the addition of the integrated heat sink [120]. Additional losses induced by the heat sink could impact the efficiency and effectiveness of this cooling solution.

Wanjiku et al. [107] designed a prototype motor that implements a flooded stator using a fiberglass casing and baffles to direct flow. The peak power was 50 kW at 7500 RPM. The authors studied three different full interwinding inlet and outlet channel designs. While the designs were similar, two had a single channel per coil, with different inlet and outlet placements. The third design had two channels per individual coil. The double cooling design saw the lowest maximum coil temperature at 175 °C, with an inlet temperature of 105 °C, 10 LPM, and ambient at 50 °C, with WEG. The rated current for this analysis was 120 A at 2000 RPM. The single-channel designs saw a maximum coil temperature of 178 °C and 205 °C for the neighboring inlet/outlet versus the dispersed inlet/outlet. However, while the dispersed inlet and outlet design saw the hottest coil temperature, the pressure drop was the lowest at 5 kPa compared to 21 and 22 kPa for the other single and double cooling channels, respectively. They also found that the coolant significantly impacted the coil temperature and pressure drop. In the same study, using the dual cooling channels with engine oil, they saw both performance metrics increase at 241 °C and 31 kPa, respectively. The motor losses were over 15 kW at the low-speed condition of 900 RPM, predominantly coming from the windings [107].

While Camilleri et al. and Wanjuku et al. implemented baffles to optimize their direct cooling designs, Liu et al. [49] used fin-like structures to direct free-flowing oil. Here, an ironless stator AFPM machine is developed with concentrated Litz wires. These oil fins are also used as the winding supporter due to removing the stator core. By removing the stator iron, the only losses in the stator are the alternating current (ac) and direct current (dc) losses. While the rotor losses (4.6 W of the 50-kW machine) and proximity losses are negligible, the major contributors are dc copper and eddy-current losses. With an inlet flow rate of 12 LPM (1.2 m/s), the flow velocity in the stator was found to be about 0.5–1 m/s. This is due to the compact, concentrated winding design, making it challenging to direct the flow. Assuming adiabatic wall conditions, the maximum end winding temperature was 100 °C, with the rest of the windings at about 70 °C for the 50-kW output. However, during the experimental testing, a temperature sensor was placed on the outer end winding and saw a steady-state temperature of about 80 °C. This was caused by natural convection, which was not present in the simulation [49].

Immersion cooling has a high coolant volume and low thermal resistance between the coolant and windings, making it an extremely effective solution. The system pressure drop is similar to in-direct solutions, such as cooling jackets, end covers, and internal flow channels, so the pumping power requirements are similar to a conventional cooling system [96], [107], [110]. Note that immersion solutions use a dielectric oil coolant, while in-direct system typically uses WEG [49], [87], [99], [100], [107], [120]. Dielectric oil coolant has poor properties and is more expensive, which will be discussed further in Section VI-A.

Few papers discuss the integration challenges of immersion cooling, including the stator case construction, structural analysis of the stator bars and casing, flow channel construction, and pressure drop requirements. In some high-power, high-RPM applications, the structural rigidity of the stator may require potting, making this solution infeasible.

E. Hollow Coils

Many conventional motor windings are manufactured with a copper bar or extruded conductors. Square cross section windings are favorable for manufacturing and achieving a high slot copper fill factor. However, these compact windings typically compromise cooling integration. Hollow coils address this issue by placing the cooling mechanism directly in the heat source [122]. Nitsche and Naderer [123] indicated that using internal flow coils allows for eliminating a water jacket leading to up to 50% more compact designs. Due to the large conductor cross section, direct cooling via hollow coils is applied in generators for power generation [124], [125], [126]. However, the availability of hollow coil extrusion and the development of additive manufacturing (AM) have made this solution more viable.

Essential system design considerations for internal flow coils include pressure drop, coil geometry, sealing integration, and electrical connections. When using hollow wire extrusion, considerations must be made for bending into shape and attaching material for electrical and thermal connections. Manufacturing via AM has also been explored due to the increased flexibility in design. Unlike extrusion, the cross

section does not need to be consistent through the coils. Furthermore, AM presents the opportunity to prototype unique cross sections and integration geometry quicker and easier.

Lindh et al. [50] designed a prototype 60-kW DSSR AFPM motor with direct cooled hollow windings. The windings consisted of hybrid hollow wire made of a stainless steel tube, with an inner diameter of 3 mm and a wall thickness of 1 mm, surrounded with Litz wire. The copper conductor and conduit were split at the terminals, and the tube was connected to insulating tubes. The copper fill factor was 37% due to the stainless tubes. The authors noted that optimization of the conductor cross section would achieve a better fill factor of the conductor. The machine consisted of two coils in parallel from a continuous 6 m length of the hybrid hollow wire. Galvanic isolation between the cooling and electrical system was achieved using a dielectric coolant and connecting nylon tubes to the stainless tubes at the end of each parallel pair. All cooling connections were made outside the stator, so leaks could be dealt with easily and would not harm the machine.

Two prototypes were evaluated by Lindh et al. [50], one which implemented direct cooling and one that did not. Eddy current losses were assessed, showing that only the tubes near the air gap were affected, and overall eddy current losses were only 5 W. At the test case of 380 Nm, 1500 RPM, and a flow rate of 6 LPM, losses for the direct cooled machine were 3.5 and 3.8 kW. The max winding temperature was 86 °C with direct cooling and 137 °C without. Water and Chemlube 221 PAO-oil were compared at the max pressure of 600 kPa. Here, the flow rate of the water was increased significantly, resulting in a 15.9 °C drop in maximum windings temp and an increase in wire current density by 3.5 times compared to the indirect prototype [50].

Documentation of prototype AFPM motors using this technology is limited to work by Lindh et al. [50], [109]. Radial flux motors have implemented this technology more widely with both extruded and AM coils seen in the literature [123], [127], [128]. This section will also discuss these radial flux designs, which could be applied to AFPM machines.

Extruded profile and hollow coils were assessed by Reinap et al. [122] in a simulation radial flux machine and a single coil test. The benefits of this cooling design were greatest during high power and overload machine operation. Analyzed conductors included a solid rectangular, hollow rectangle with a hole, and a profiled "U" in vertical and horizontal orientations. The hollow and profiled U conductors had a cross-sectional area of 8.3 mm^2, while the solid conductor, with identical outer dimensions, had a cross section of 11.4 mm^2. Copper losses in the windings were the machine's most significant losses, and the current density reached 100 A/mm^2 in some locations. Losses in the solid conductor were 1912 W compared to 2619 W in the directly cooled conductor. The authors tested transformer and engine oil at a flow rate of 0.7 LPM and a heat power of 60 m/cm^3, the max conductor temp being 109 °C and 99.8 °C, respectively. Testing showed that continuous operation of the machine could be safely performed at higher current densities (40 A/mm^2 and above) with the direct cooling of the conductor [122].

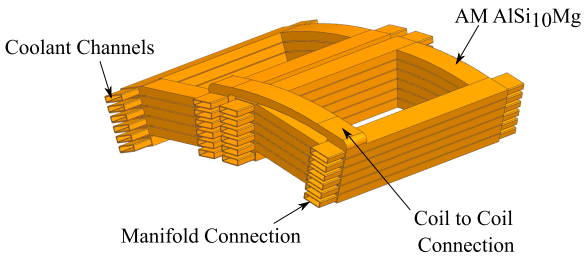

Fig. 15. Additively manufactured hollow conductor for radial flux machine [127].

Wu and EL-Refaie [127] presented an AM hollow coil design and validated it in a radial flux 250-kW prototype motor for a passenger aircraft hybrid powertrain. The machine achieved a specific power of 20.17 kW/kg and an efficiency of 95.89%. The coils are aluminum alloy $AlSi_10Mg$ manufactured through direct metal laser sintering (DMLS) AM. The aluminum alloy is 70% lighter but 40% more resistive than a copper alloy. The windings were cooled below 110 °C at the steady-state operation (85 kW) despite a winding loss of 5.7 kW. The coolant channels run along the coil lengths and are connected in parallel with a manifold, as shown in Fig. 15. Each parallel path had a flow rate of 0.057 LPM reducing the pressure drop significantly as channel openings were only about 1 mm wide [127]. A challenge with AM parts is balancing surface roughness for increased heat transfer and pressure drop through the system. $AlSi_10Mg$ samples can have surface roughness from 6 to 94 μm depending on the surface angle and printing parameters [129], [130]. High roughness can dramatically increase the pressure drop through small channels like those described by Wu and EL-Refaie [127].

Wohlers et al. [128] created two conductor cross sections that optimize current density throughout the winding and maximized surface area. The first is a "U" profile coil, which can be cast. The second consists of holes, curves, and cutouts, which can only be made through AM, as shown in Fig. 16. The shape of the conductor cross section increases the homogeneity of the current density distribution within the conductors, decreasing losses. The authors compared their first design to a solid square conductor and showed that their design could reduce losses by 50% and achieve a current density of 100 A/mm^2 without exceeding the coil max insulation temperature of 180 °C. This reduction in losses allows for a broader range of operating frequency and current, increasing the power of the machine. A prototype AM coil was made through DMLS of $AlSi_{10}Mg$ and tested with deionized water coolant. The test results were in agreement with the simulation results. Calculations determined the maximum current density for this coil to be 130 A/mm^2 when flood cooled by deionized water [128].

Hollow coils present a direct cooling solution that allows potting of the stator for increased structural rigidity and, when combined with immersion, can increase current density dramatically. Compared to in-direct solutions, increased allowable current density and an integrated thermal management system will decrease motor size. This concept also has versatility as hollow coils could be used in all AFPM motor topologies.

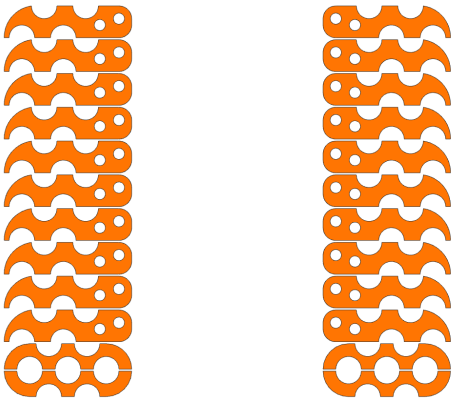

Fig. 16. Additively manufactured profiled conductor cross section [128].

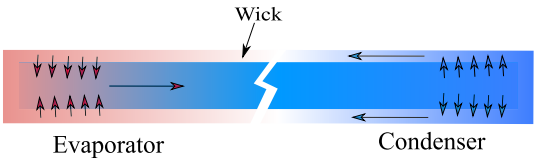

Fig. 17. Copper-water HP diagram [131].

However, hollow coils inherently have a poorer copper fill factor than solid coils, meaning that the stator may be bigger than immersion solutions with concentrated windings. Furthermore, high system pressure drop can occur due to the high viscosity of the dielectric coolant and the small channel size. Lindh et al. [50] recorded pump pressures up to 600 kPa, requiring a larger pump, increasing system mass and parasitic losses. Over the motor's lifetime, pumping power requirements may increase significantly due to fowling in the small channels although more research is required.

F. Heat Pipes

HPs are efficient heat transport devices that use a phase change fluid. Their equivalent thermal conductivity can reach 100 000 W/mK [131], making them ideal for thermal management in high-power electric machines. Prototype machines implementing this technology have seen improvements in thermal management and power density [110], [132], [133], [134], [135], [136], [137]. However, Le et al. [110] and Mueller et al. [136] present the only use in AFPM motors seen in the literature. Despite their high heat transfer efficiency, the use of HPs in commercial electric machines has been limited due to cost and reliability [131], [132]. Studies noted challenges with increased power losses when adding HPs to the stator. However, recent developments in additive manufacturing and advanced materials could soon make this technology a more practical cooling solution.

Wicked HPs are the most popular for use in electric machines. There are many types of wicks; however, conventionally manufactured meshed wicks are usually chosen for their compromise between cost and performance [131], [132]. In an HP, there are two sides: the hot side, the evaporator, and the cold side, the condenser, as shown in Fig. 17. Ambient heat evaporates the fluid, forcing it down the pipe to the condenser.

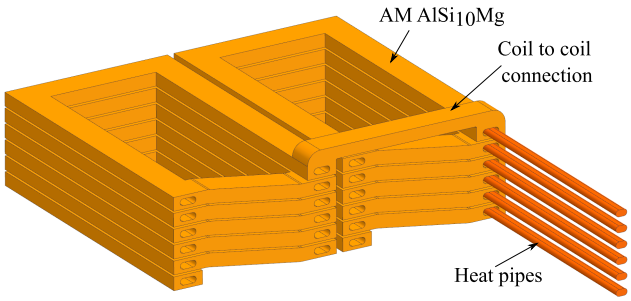

Fig. 18. Additively manufactured coils with integrated HP [139].

The vapor then condenses into the wick and travels back to the evaporator. Wicks must be carefully designed for the intended operating limits to prevent "dry-out." "Dry-out" can occur when the heat flux on the hot side is too high or when the pumping pressure drop is less than the gravitational, liquid, and vapor pressure [131]. Alternatively, if the heat flux is too low for the phase change fluid to vaporize, the HP will exhibit the thermal conductivity of the shell material [110]. For this reason, it is critical to carefully choose the phase change fluid, HP casing material, and wick type for the intended operating conditions and temperatures.

Failure in HPs is typically caused by issues during manufacturing or improper design for the intended application. These issues include insufficient cleaning of the interior, improper filling, leakage, incompatible materials, dry-out, and incorrect orientation with respect to gravity. These issues could lead to poor reliability of the HP and, therefore, motor [138].

Le et al. [110] designed an AFPM motor for electric vehicles. The thermal management system consists of a water jacket, as described above, and flat HPs situated between the stator slots. The HPs are 2 × 8 × 85 mm with a copper casing and water as the working fluid. The equivalent thermal conductivity achieved was 70 000 W/(mK) within a temperature range of 80 °C–110 °C [110].

Wu et al.'s [139] work shows the integration of HPs inside an AM coil for a radial flux machine, as shown in Fig. 18. The addition of the HP improves cooling capabilities. However, the HP and conductor are separate parts that cause losses to increase by 8% compared to a coil without the HP [139].

In the AM space, materials such as polymers and ceramics have been explored for manufacturing HPs as they do not induce additional losses in the motor. However, these materials are far less effective due to reduced material conductivity and increased contact resistance.

Szymanski and Mikielewicz [140] developed an aluminum alloy ammonia HP with a hybrid sintered wick using DMLS. AM allowed researchers to fine-tune the wick geometry in ways that would be impossible using conventional manufacturing methods. The optimized wick decreased pressure drop without compromising capillary pumping capacity and achieved a 10% increase in heat transfer compared to the equivalent conventional HP. The study also tested a variety of wick structures and compared densities and geometries. The authors noted that predicting the mechanical properties

of these AM HPs is challenging, and research still needs to be done to understand these parameters [140].

Further research must be done in the additive manufacturing space to understand the impact of printing parameters and powder size on the thermal performance of HP. One future direction of high-performance motors in HP technology is printing HP geometry in stator windings. Combining the conductor and HP will eliminate additional losses created as separate parts and maximize the thermal management system's thermal conductivity.

The induced losses and reliability issues in HPs should be addressed when considering this thermal management solution. Furthermore, the HP condenser system will also need to be designed. Le et al. [110] implemented a water jacket, increasing the weight and volume of the motor design.

VI. Materials and Coolants

A. Coolants

Dielectric coolants are typically low-viscosity oils used for direct cooling applications. The benefits of these coolants are that they do not form ions, provide insulation in stator flooding configurations, and conduct heat away from the source. Oil-based coolants have a lower heat capacity and higher viscosity than water-based coolants making coolant selection critical for each use case. Synthetic oils, including those in Table IV [141], [142], [143], [144], [145], [146], [147], are less sensitive to sludging or fouling from thermal oxidization, making them a more favorable choice in direct cooling systems.

Deionized water can also be used; however, the fluid contact materials must be carefully assessed as deionized water can quickly form ions [50]. Water-based coolants, such as WEG, are typically used for indirect cooling due to their high thermal conductivity and low viscosity. These applications usually do not need a dielectric fluid. Table IV lists available coolants for liquid cooling and their properties. This is in no way a comprehensive list of all available coolants. Other coolants reported in the literature include Galden HT 135 [141] and Syltherm 800 [142], as well as engine and compressor oil in experimental setups [50], [128].

Coolant selection should consider direct cooling performance characteristics, such as thermal conductivity and system-level thermal management, for example, weight, pumping power, material compatibility, and maximum allowable temperature. YASA Ltd. [18] floods the stator with OptiCool-H [143], which has a density less than water, decreasing the weight of the thermal management system. However, the maximum coolant temp is only 130 °C, which could limit the duration of peak power.

It should also be noted that synthetic oil properties fluctuate significantly depending on temperature. For example, the viscosity of AmpCool[1] AC-110 is 41.10 cSt at 0 °C, 8.11 at 40 °C, and 2.22 at 100 °C [146]. High coolant viscosity at low temperatures will have implications for the pumping power required and could require a system warm-up period.

[1]Registered trademark.

B. Encapsulants

Encapsulating the stator is common in high power high torque AFPM machines to provide a thermal path from the conductors to the housing and for structural rigidity. Typical potting materials have poor thermal conductivity (less than 1 W/mK) and have maximum operating temperatures of around 180 °C [151]. The filler materials are added to the potting material matrix to manipulate the material properties.

Glass is added to increase mechanical properties at the cost of thermal conductivity. Metallic filler materials increase thermal conductivity while decreasing mechanical and insulative properties [118]. Metallic materials typically have a higher density than matrix material, causing increased machine weight. Furthermore, adding filler in general increases the potting material viscosity and could cause challenges during encapsulation, leading to air pockets [151]. Thermal conductivities of over 4 W/mk have been reported; however, above this value, there can be issues with viscosity and diminishing increases in thermal management performance [151], [152].

VII. Future Trends and Innovations

Our team is currently working on the development of additively manufactured (AM) hollow conductor technology (copper and aluminum). As explained in Section V-E, hollow conductors represent a very promising cooling system approach, and the recent improvements in AM open new scenarios considered impossible just a few years ago. Despite its efficiency, the AM hollow coils pose several challenges from the electrical, manufacturing, and fluid-dynamics standpoints. The first problem to be solved is electrical conductivity. Most of the copper powder alloys have an IACS not as high as extruded copper. Recently, some important academic and industrial effort has been made to support pure copper printing by means of new green laser technology, but the large-scale availability is still far. Another issue is the uniformity of the conductivity. The electric machine phases need to have a well-balanced resistance. A highly controlled manufacturing process is crucial to ensure consistent physical properties. Again, great progress has been made in the control of these properties during the 3-D-printing and the postprocessing such as heat treatments, but the traditional wire extrusion is still a standard reference. AM, however, has one important advantage compared to the extruded hollow or solid bar conductors: the minimization of the welding joints. By enabling the realization of complex geometries in a single piece instead of multiple parts, AM makes it possible to print sets of coils and, eventually, the whole winding without the need for welding. The welding of conventional coils is a source of uneven electrical extra resistance, which can cause unbalanced phases and hot spots in the winding. Porosity is also a well-known problem of metal 3-D-printing and, in the context of the hollow conductors, becomes particularly important. The porosity, in fact, can not only raise the resistance of the hollow conductor regardless of the metal powder utilized but also compromise the sealing of the liquid cooling circuit. Highly accurate laser power settings are, therefore, essential. Dimensional stability is, finally, the last main factor for the AM hollow coils to

TABLE IV
COOLANTS USED FOR STATOR THERMAL MANAGEMENT

Product	Manufacturer	Coolant Base	Density (kg/m^3)	Viscosity (cSt)	Thermal Conductivity (W/mK)	Max Temp (°C)	Dielectric Constant
OptiCool-H [143]	DSI Venture, Inc.	Hydrotreated Paraffin Oil	825 @16 °C	1.4 @100 °C	0.1344 @100 °C	130	Low
Opteon SF10 [144]	Chemours	Florinated Fluid	1580	0.71 @25 °C	0.077 @25 °C	110	Low
Novec 7500 [145]	3M™	Fluorocarbon Oil	1630 @20 °C	0.71 @25 °C	0.0591	128	Low
AmpCool AC-110 [146]	Engineered Fluids	Synthetic Oil	8200 @15 °C	2.22 @100 °C	0.1325 @100 °C	180	2.08
THERMINOL 68 [147]	Eastman Chemical Company	Synthetic Oil	969 @100 °C	0.26 @100 °C	0.117 @100 °C	360	2.8 @23 °C
Ethylene Glycol [148]	—	Hygroscopic Liquid	1113 @20 °C	19.83 @20 °C	—	187*	37.7 @25 °C
Deionized Water† [149], [150]	—	Water	997 @25 °C	1 @20 °C	0.606 @25 °C	99.9*	80 @25 °C

* Coolant boiling point

† To be used as a reference point

succeed. The mechanical tolerances achievable by means of extrusion are still way better than those of 3-D-printing, as well as the surface roughness. In order to maximize the copper fill factor, the distances between different coils, or consecutive turns, or between the coil and the stator bar are usually tight. Without extremely precise control of the geometric tolerances, the coils might not be able to fit in the full machine assembly, and the scrap rate can become industrially unbearable. Besides, unexpected variations in the cooling channel size would have adverse effects on the pressure drop, already high in this particular cooling system design. The AM has also another geometry-consistency issue, the warpage, which, in the special case of the electrical coils, results in some sort of twisted shape. Of course, that is not acceptable, but heat treatments can be highly beneficial from this point of view. On the other hand, the AM removes the problem of the maximum bending radius, which affects the extruded hollow conductors. In conclusion, the AM hollow conductor can be one of the key technologies to increase the electric current density, and therefore the power density, of the new generation AFPMs, but scientific research still needs to find solutions to several technical challenges.

VIII. CONCLUSION

Thermal management for AFPM is the most challenging design aspect and is often the limiting factor in increasing machine capabilities. The rotor magnets and stator conductors are the two most dominant electromagnetic loss sources in AFPM motors. Cooling these components is crucial to achieving the ambitious requirements of heavy-duty vehicles and aerospace applications.

The SSDR topology is selected by AFE motors, Emrax, Evolito, MagnaX, and YASA Ltd., whereas the DSSR was chosen by AVID, MAGELEC, and Phi Power, as shown in Table I. It would be challenging to compare these electric motors' thermal management system performance as it varies considerably depending on the configuration, loss distribution between stator and rotor, main operating point, and the intended application. Nevertheless, some conclusions can be made about the general trends.

Section II-B explains that the baseline DSSR configuration has a higher mass than the SSDR (YASA) due to two stator yokes and the additional end-winding length. For this reason, the companies that use DSSR tend to increase the maximum speed to compensate for this disadvantage. The single rotor is theoretically symmetrical, and the magnetic load in DSSR is also more balanced than in SSDR, as the rotor is between two identical stators. The higher speed enables these companies to reduce the torque needed for the same power rating, downsizing the machine.

A major challenge of DSSR motors is the cooling system design. First, air-cooling conditions for the rotor are poorer, and generally, the cooling enhancements discussed in Section IV are not feasible. Magnetic loss in the rotor is typically higher due to higher electric frequency caused by higher speeds. Distributed windings are adopted instead of FSCW to decrease these losses. However, their small diameter and greater number of slots make it challenging to utilize direct cooling methods. The slots are typically too small for cooling channels, and the stator yokes prevent stator cooling via immersion. The most prevalent cooling system of DSSR

is indirect cooling by end cover jackets, as discussed in Section V-A2. Here, the thermal contact resistance with the windings is inherently worse than with direct methods, and the axial length of the motor is increased.

DSSR operating at higher speeds also has consequences on the motor application. Lower speed SSDR can achieve high power density and high torque density simultaneously, thus suitable for direct-drive. In contrast, higher speed DSSR usually requires more complicated gearboxes with higher ratios, adversely affecting the vehicle's overall mass, cost, reliability, and efficiency.

Rotor cooling is essential to prevent reversible and irreversible demagnetization of the magnets. The double-rotor configuration is typically air-cooled with rotor blades. Depending on cooling requirements, fins, vents, and mesh structures can be used to increase the heat transfer coefficient of the rotor carrier. Studies have shown that these air-cooling features can be optimized to minimize windage losses, maximize the cooling effect, and prevent demagnetization.

In addition, stator cooling can be accomplished by several strategies, including jackets, fins, channels, immersion cooling, hollow coils, and HPs. To improve the cooling performance of the design and increase the power density, the chosen solution should consider integration between two or more of these thermal technologies. For example, a water jacket, one of the most popular solutions, significantly increases the motor size and may not provide sufficient cooling depending on the machine's power density and losses. Depending on the machine topology, the most successful strategy seen in commercial AFPM machines is immersion cooling. Enhancements to these flooded concepts, such as baffles, extended heat transfer surfaces and hollow coils, and further improve cooling capabilities.

With the increasing demand for high-power electric machines, innovative thermal management technologies must be thoroughly investigated. Rotor blades and stator immersion cooling in SSDR configurations show promising results and have started to see commercial success. Additively manufactured hollow or profiled conductors show promise in increasing current density, and therefore, power density indicating machines for the new stage of transportation electrification will be achievable in the future. Further research should investigate the testing, validation, and long-term reliability of these emerging solutions in prototype machines. The challenges associated with integration should also be studied to understand which strategies may see better success in commercial high-performance AFPM motors. Several technologies, however, show promising results, indicating that machines for the new stage of transportation electrification will be achievable.

REFERENCES

[1] (2021). *Global EV Outlook 2021*. IEA, Paris, France. [Online]. Available: https://www.iea.org/reports/global-ev-outlook-2021

[2] Daimler. (Dec. 2021). *Ecascadia*. [Online]. Available: https://freightliner.com/trucks/ecascadia/

[3] I. Meritor. (Dec. 2021). *Meritor Epowertrains*. [Online]. Available: https://www.meritor.com/products/epowertrains/

[4] K. Trucks. (Dec. 2021). *T680e*. [Online]. Available: https://www.kenworth.com/trucks/t680e/

[5] D. Speth and S. Á. Funke, "Comparing options to electrify heavy-duty vehicles: Findings of German pilot projects," *World Electr. Vehicle J.*, vol. 12, no. 2, p. 67, Apr. 2021.

[6] A. Kampker, K. Krciskother, M. K. Buning, and J. G. Dorantes Gomez, "Technological and total cost of ownership analysis of electric powertrain concepts for long-haul transport in comparison to traditional powertrain concepts," in *Proc. 8th Int. Electric Drives Prod. Conf. (EDPC)*, Schweinfurt, Germany, Dec. 2018, pp. 1–7.

[7] H. Won, Y.-K. Hong, J. Platt, M. Choi, B. Bryant, and S. Choi, "Six-phase fractional-slot concentrated winding ferrite spoke-type permanent magnet synchronous motor for electric truck," in *Proc. IEEE Int. Electric Mach. Drives Conf. (IEMDC)*, Hartford, CT, USA, May 2021, pp. 1–6.

[8] J.-W. Chin, K.-S. Cha, M.-R. Park, S.-H. Park, E.-C. Lee, and M.-S. Lim, "High efficiency PMSM with high slot fill factor coil for heavy-duty EV traction considering AC resistance," *IEEE Trans. Energy Convers.*, vol. 36, no. 2, pp. 883–894, Jun. 2021.

[9] (2021). *Evolito Ltd*. [Online]. Available: https://evolito.aero/technology/

[10] J. Benzaquen, J. He, and B. Mirafzal, "Toward more electric powertrains in aircraft: Technical challenges and advancements," *CES Trans. Electr. Mach. Syst.*, vol. 5, no. 3, pp. 177–193, Sep. 2021.

[11] A. S. Fawzal, R. M. Cirstea, T. J. Woolmer, M. Dickison, M. Blundell, and K. N. Gyftakis, "Air inlet/outlet arrangement for rotor cooling application of axial flux PM machines," *Appl. Thermal Eng.*, vol. 130, pp. 1520–1529, Feb. 2018.

[12] (2021). *AFE Motors*. [Online]. Available: https://www.afe-motors.com/

[13] (2021). *Avid Ltd*. [Online]. Available: https://avidtp.com/product/evo-motors/

[14] (2021). *Emrax D.O.O*. [Online]. Available: https://emrax.com/

[15] (2021). *Magelec Ltd*. [Online]. Available: http://www.magelec.cn/en/

[16] (2021). *Magnax BV*. [Online]. Available: https://www.magnax.com/

[17] (2021). *Phi-Power AG*. [Online]. Available: https://www.phi-power.com/

[18] (2021). *Yasa Ltd*. [Online]. Available: https://www.yasa.com/

[19] J. Gieras, R. Wang, and M. Kamper, *Axial Flux Permanent Magnet Brushless Machines*. Amsterdam, The Netherlands: Springer, 2008.

[20] N. Taran, G. Heins, V. Rallabandi, D. Patterson, and D. M. Ionel, "Torque production capability of axial flux machines with single and double rotor configurations," in *Proc. IEEE Energy Convers. Congr. Expo. (ECCE)*, Sep. 2018, pp. 7336–7341.

[21] N. Taran, V. Rallabandi, G. Heins, and D. M. Ionel, "Systematically exploring the effects of pole count on the performance and cost limits of UltraHigh efficiency fractional hp axial flux PM machines," *IEEE Trans. Ind. Appl.*, vol. 56, no. 1, pp. 117–127, Jan. 2020.

[22] (2021). *Axial Flux Motor Market Forecast (2021–2026)*. [Online]. Available: https://www.industryarc.com/Report/19433/axial-flux-motor-market.html

[23] F. Giulii Capponi, G. De Donato, and F. Caricchi, "Recent advances in axial-flux permanent-magnet machine technology," *IEEE Trans. Ind. Appl.*, vol. 48, no. 6, pp. 2190–2205, Nov. 2012.

[24] W. Fei, "Permanent magnet synchronous machines with fractional slot and concentrated winding configurations," Ph.D. dissertation, Dept. Eng. Appl. Sci., Cranfield Univ., Cranfield, U.K., 2011.

[25] C. Du-Bar, "Design of an axial flux machine for an in-wheel motor application," M.S. thesis, Dept. Energy Environ., Chalmers Univ. Technol., Goteborg, Sweden, 2011.

[26] T. Husain, B. Tekgun, Y. Sozer, and M. Hamdan, "Comparison of axial flux machine performance with different rotor and stator configurations," in *Proc. IEEE Int. Electr. Mach. Drives Conf. (IEMDC)*, Miami, FL, USA, May 2017, pp. 1–8.

[27] R. D. Chavan and V. N. Bapat, "The study of different topologies of axial flux permanent magnet generator," in *Proc. Int. Conf. Autom. Control Dyn. Optim. Techn. (ICACDOT)*, Pune, India, Sep. 2016, pp. 202–206.

[28] M. Aydin and M. Gulec, "Reduction of cogging torque in double-rotor axial-flux permanent-magnet disk motors: A review of cost-effective magnet-skewing techniques with experimental verification," *IEEE Trans. Ind. Electron.*, vol. 61, no. 9, pp. 5025–5034, Sep. 2014.

[29] N. J. Stannard, J. G. Washington, and G. J. Atkinson, "A comparison of axial field topologies employing SMC for traction applications," in *Proc. 19th Int. Conf. Elect. Mach. Syst. (ICEMS)*, Chiba, Japan, Nov. 2016, pp. 1–6.

[30] A. Mahmoudi, H. Wooi Ping, and N. A. Rahim, "A comparison between the TORUS and AFIR axial-flux permanent-magnet machine using finite element analysis," in *Proc. IEEE Int. Electr. Mach. Drives Conf. (IEMDC)*, Niagara Falls, ON, Canada, May 2011, pp. 242–247.

[31] M. Aydin, S. Huang, and T. A. Lipo, "Design and 3D electromagnetic field analysis of non-slotted and slotted TORUS type axial flux surface mounted permanent magnet disc machines," in *Proc. IEEE Int. Electr. Mach. Drives Conf. (IEMDC)*, Cambridge, MA, USA, Jun. 2001, pp. 645–651.

[32] S. Huang, M. Aydin, and T. A. Lipo, "TORUS concept machines: Pre-prototyping design assessment for two major topologies," in *Proc. Conf. Rec. IEEE Ind. Appl. Conf. 36th IAS Annu. Meeting*, vol. 3, Sep./Oct. 2001, pp. 1619–1625.

[33] L. Xu, X. Zhu, W. Fan, C. Zhang, L. Zhang, and L. Quan, "Comparative analysis and design of partitioned stator hybrid excitation axial flux switching PM motors for in-wheel traction applications," *IEEE Trans. Energy Convers.*, vol. 37, no. 2, pp. 1416–1427, Jun. 2022.

[34] R. Di Stefano and F. Marignetti, "Electromagnetic analysis of axial-flux permanent magnet synchronous machines with fractional windings with experimental validation," *IEEE Trans. Ind. Electron.*, vol. 59, no. 6, pp. 2573–2582, Jun. 2012.

[35] N. Bianchi, S. Bolognani, and E. Fornasiero, "An overview of rotor losses determination in three-phase fractional-slot PM machines," *IEEE Trans. Ind. Appl.*, vol. 46, no. 6, pp. 2338–2345, Nov. 2010.

[36] A. Cavagnino, M. Lazzari, F. Profumo, and A. Tenconi, "A comparison between the axial flux and the radial flux structures for PM synchronous motors," *IEEE Trans. Ind. Appl.*, vol. 38, no. 6, pp. 1517–1524, Nov./Dec. 2002.

[37] H. Zhang, H. Zhou, and R. Pei, "Investigation of axial-flux permanent magnet machine with strap-wire and segmented magnet for logistics electric vehicle," in *Proc. IEEE Int. Magn. Conf. (INTERMAG)*, Lyon, France, Apr. 2021, pp. 1–5.

[38] C. Wang, R. Qu, J. Li, X. Fan, D. Li, and Y. Lu, "Rotor loss calculation and thermal analysis of a dual-stator axial-flux permanent magnet machine with combined rectangle-shaped magnets," in *Proc. 20th Int. Conf. Electr. Mach. Syst. (ICEMS)*, Sydney, NSW, Australia, Aug. 2017, pp. 1–5.

[39] Q. Chen, D. Liang, S. Jia, Q. Ze, and Y. Liu, "Loss analysis and experiment of fractional-slot concentrated-winding axial flux PMSM for EV applications," in *Proc. IEEE Energy Convers. Congr. Expo. (ECCE)*, Sep. 2018, pp. 4329–4335.

[40] A. Hemeida, P. Sergeant, and H. Vansompel, "Comparison of methods for permanent magnet eddy-current loss computations with and without reaction field considerations in axial flux PMSM," *IEEE Trans. Magn.*, vol. 51, no. 9, pp. 1–11, Sep. 2015.

[41] I. Petrov, M. Polikarpova, P. Ponomarev, P. Lindh, and J. Pyrhonen, "Investigation of additional AC losses in tooth-coil winding PMSM with high electrical frequency," in *Proc. XXII Int. Conf. Electr. Mach. (ICEM)*, Lausanne, Switzerland, Sep. 2016, pp. 1841–1846.

[42] R. Phillips and D. T. Woolmer, "AC copper losses in edge-wound coils in a YASA motor," in *Proc. 10th Int. Conf. Power Electron., Mach. Drives (PEMD)*, 2021, pp. 746–751.

[43] S. G. Min and B. Sarlioglu, "Analysis and comparative study of flux weakening capability in fractional-slot concentrated windings," *IEEE Trans. Energy Convers.*, vol. 33, no. 3, pp. 1025–1035, Sep. 2018.

[44] L. Junlong, X. Yongxiang, Z. Jibin, W. Baochao, W. Qian, and L. Weiyan, "Analysis and design of SPM machines with fractional slot concentrated windings for a given constant power region," *IEEE Trans. Magn.*, vol. 51, no. 11, pp. 1–4, Nov. 2015.

[45] A. M. El-Refaie, Z. Q. Zhu, T. M. Jahns, and D. Howe, "Winding inductances of fractional slot surface-mounted permanent magnet brushless machines," in *Proc. IEEE-IAS*, Edmonton, AB, Canada, Oct. 2008, pp. 1–8.

[46] R. Ni, G. Wang, X. Gui, and D. Xu, "Investigation of d- and q-axis inductances influenced by slot-pole combinations based on axial flux permanent-magnet machines," *IEEE Trans. Ind. Electron.*, vol. 61, no. 9, pp. 4539–4551, Sep. 2014.

[47] W. Jara, P. Lindh, J. Tapia, and J. Pyrhonen, "A novel rotor structure for an axial flux PM machine: Performance analysis," in *Proc. Int. Symp. Power Electron., Electr. Drives, Autom. Motion (SPEEDAM)*, Capri, Italy, Jun. 2016.

[48] J. H. Kim, W. Choi, and B. Sarlioglu, "Closed-form solution for axial flux permanent-magnet machines with a traction application study," *IEEE Trans. Ind. Appl.*, vol. 52, no. 2, pp. 1775–1784, Mar./Apr. 2016.

[49] Y. Liu, Z. Zhang, C. Wang, W. Geng, and T. Yang, "Design and analysis of oil-immersed cooling stator with nonoverlapping concentrated winding for high-power ironless stator axial-flux permanent magnet machines," *IEEE Trans. Ind. Electron.*, vol. 68, no. 4, pp. 2876–2886, Apr. 2021.

[50] P. Lindh et al., "Direct liquid cooling method verified with an axial-flux permanent-magnet traction machine prototype," *IEEE Trans. Ind. Electron.*, vol. 64, no. 8, pp. 6086–6095, Mar. 2017.

[51] M. Abdalmagid, G. Pietrini, A. Callegaro, M. Goykhman, and A. Emadi, "Bearing current modelling and investigation in axial flux permanent magnet synchronous motors for aerospace applications," in *Proc. IEEE Transp. Electrific. Conf. Expo (ITEC)*, Anaheim, CA, USA, Jun. 2022, pp. 1–6.

[52] D. Talebi, M. C. Gardner, S. V. Sankarraman, A. Daniar, and H. A. Toliyat, "Electromagnetic design characterization of a dual rotor axial flux motor for electric aircraft," *IEEE Trans. Ind. Appl.*, vol. 58, no. 6, pp. 7088–7098, Nov. 2022.

[53] Y. Yu, Z. Hao, Y. Bi, and Y. Pei, "Performance analysis between grain-oriented and non-oriented material on yokeless and segmented armature machine," in *Proc. 22nd Int. Conf. Electr. Mach. Syst. (ICEMS)*, Harbin, China, Aug. 2019, pp. 1–5.

[54] D. Kowal, P. Sergeant, L. Dupre, and A. Van den Bossche, "Comparison of nonoriented and grain-oriented material in an axial flux permanent-magnet machine," *IEEE Trans. Magn.*, vol. 46, no. 2, pp. 279–285, Feb. 2010.

[55] T. Sebastian, "Temperature effects on torque production and efficiency of PM motors using NdFeB magnets," *IEEE Trans. Ind. Appl.*, vol. 31, no. 2, pp. 353–357, Mar. 1995.

[56] (2021). *Bomatec Magnets*. [Online]. Available: https://www.bomatec.com/en/products/

[57] W. Sixel, M. Liu, and B. Sarlioglu, "Rotor thermal design for electric machines: Challenges and opportunities," in *Proc. IEEE Transp. Electrific. Conf. Expo (ITEC)*, Long Beach, CA, USA, Jun. 2018, pp. 821–826.

[58] G. K. Batchelor, "Note on a class of solutions of the Navier-Stokes equations representing steady rotationally-symmetric flow," *Quart. J. Mech. Appl. Math.*, vol. 4, no. 1, pp. 29–41, 1951.

[59] K. Stewartson, "On the flow between two rotating coaxial disks," *Math. Proc. Cambridge Phil. Soc.*, vol. 49, no. 2, pp. 333–341, Apr. 1953.

[60] G. L. Mellor, P. J. Chapple, and V. K. Stokes, "On the flow between a rotating and a stationary disk," *J. Fluid Mech.*, vol. 31, no. 1, pp. 95–112, Jan. 1968.

[61] J. F. Brady and L. Durlofsky, "On rotating disk flow," *J. Fluid Mech.*, vol. 175, pp. 363–394, Feb. 1987.

[62] J. W. Daily and R. E. Nece, "Chamber dimension effects on induced flow and frictional resistance of enclosed rotating disks," *J. Basic Eng.*, vol. 82, no. 1, pp. 217–230, Mar. 1960.

[63] S. Poncet, R. Schiestel, and M.-P. Chauve, "Centrifugal flow in a rotor-stator cavity," *J. Fluids Eng.*, vol. 127, no. 4, pp. 787–794, Jul. 2005.

[64] S. Poncet, M. P. Chauve, and P. Le Gal, "Turbulent rotating disk flow with inward throughflow," *J. Fluid Mech.*, vol. 522, pp. 253–262, Jan. 2005.

[65] E. C. Cobb and O. Saunders, "Heat transfer from a rotating disc," *Amer. Soc. Mech. Eng.*, vol. 236, no. 1206, pp. 343–351, Aug. 1956.

[66] L. Dorfman, *Hydrodynamic Resistance and the Heat Loss of Rotating Solids*. Edinburgh, U.K.: Oliver & Boyd, 1963.

[67] J. M. Owen and R. H. Rogers, "Flow and heat transfer in rotating-disc systems. Volume I—Rotor-stator systems," NASA STI/Recon, Tech. Rep. A 90, 1989, p. 45759.

[68] S. L. Soo, "Laminar flow over an enclosed rotating disk," *Trans. ASME*, vol. 80, no. 2, pp. 287–296, 1958.

[69] V. M. Kapinos, "Heat transfer from a disc rotating in a housing with a radial flow of coolant," *J. Eng. Phys.*, vol. 8, no. 1, pp. 35–38, Jan. 1965.

[70] J. M. Owen, "The Reynolds analogy applied to flow between a rotating and a stationary disc," *Int. J. Heat Mass Transf.*, vol. 14, no. 3, pp. 451–460, Mar. 1971.

[71] R. Boutarfa and S. Harmand, "Local convective heat transfer for laminar and turbulent flow in a rotor-stator system," *Exp. Fluids*, vol. 38, no. 2, pp. 209–221, Feb. 2005.

[72] A. Rasekh, P. Sergeant, and J. Vierendeels, "Fully predictive heat transfer coefficient modeling of an axial flux permanent magnet synchronous machine with geometrical parameters of the magnets," *Appl. Thermal Eng.*, vol. 110, pp. 1343–1357, Jan. 2017.

[73] D. A. Howey, A. S. Holmes, and K. R. Pullen, "Measurement and CFD prediction of heat transfer in air-cooled disc-type electrical machines," *IEEE Trans. Ind. Appl.*, vol. 47, no. 4, pp. 1716–1723, Jul. 2011.

[74] G. Airoldi et al., "Air flow and heat transfer modeling of an axial flux permanent magnet generator," *World Acad. Sci., Eng. Technol.*, vol. 58, pp. 809–813, 2009.

[75] D. A. Howey, P. R. N. Childs, and A. S. Holmes, "Air-gap convection in rotating electrical machines," *IEEE Trans. Ind. Electron.*, vol. 59, no. 3, pp. 1367–1375, Mar. 2012.

[76] R. E. Nece and J. W. Daily, "Roughness effects on frictional resistance of enclosed rotating disks," *J. Basic Eng.*, vol. 82, no. 3, pp. 553–560, Sep. 1960.

[77] J. Owen and C. Haynes, "Design formulae for the heat loss and frictional resistance of air-cooled rotating discs," *Improvements Fluid Mach. Syst. Energy Convers.*, vol. 4, p. 127, Apr. 1976.

[78] A. Rasekh, P. Sergeant, and J. Vierendeels, "A parametric-CFD study for heat transfer and fluid flow in a rotor-stator system," in *11th World Congress Comput. Mech., 5th Eur. Conf. Comput. Mech., 6th Eur. Conf. Comput. Fluid Dyn. (WCCM/ECCM/ECFD)*, 2014.

[79] Y. C. Chong, E. J. P. E. Subiabre, M. A. Mueller, J. Chick, D. A. Staton, and A. S. McDonald, "The ventilation effect on stator convective heat transfer of an axial-flux permanent-magnet machine," *IEEE Trans. Ind. Electron.*, vol. 61, no. 8, pp. 4392–4403, Aug. 2014.

[80] H. Vansompel, "Design of an energy efficient axial flux permanent magnet machine," Ph.D. dissertation, Ghent Univ., Ghent, Belgium, 2013.

[81] A. S. Fawzal, R. M. Cirstea, K. N. Gyftakis, T. J. Woolmer, M. Dickison, and M. Blundell, "Fan performance analysis for rotor cooling of axial flux permanent magnet machines," *IEEE Trans. Ind. Appl.*, vol. 53, no. 4, pp. 3295–3304, Jul. 2017.

[82] A. S. Fawzal, R. M. Cirstea, K. N. Gyftakis, T. J. Woolmer, M. Dickison, and M. Blundell, "The fan design impact on the rotor cooling of axial flux permanent magnet machines," in *Proc. XXII Int. Conf. Electr. Mach. (ICEM)*, Sep. 2016, pp. 2725–2731.

[83] F. N. U. Nishanth, G. Bohach, M. M. Nahin, J. Van De Ven, and E. L. Severson, "Design of an axial flux machine with an integrated hydraulic pump for off-highway vehicle electrification," in *Proc. IEEE Energy Convers. Congr. Expo. (ECCE)*, Detroit, MI, USA, Oct. 2020, pp. 1772–1779.

[84] H. Chuan, R. Burke, and Z. Wu, "A comparative study on different cooling topologies for axial flux permanent magnet machine," in *Proc. IEEE Vehicle Power Propuls. Conf. (VPPC)*, Hanoi, Vietnam, Oct. 2019, pp. 1–6.

[85] I. Zaher, R. Rodriguez, E. Sayed, A. Callegaro, M. Goykhman, and A. Emadi, "Effect of rotor geometry on rotor air cooling of a ventilated axial-flux permanent magnet machine," in *Proc. IEEE Transp. Electrific. Conf. Expo (ITEC)*, Jun. 2021, pp. 77–82.

[86] H. Yan, W.-T. Wu, S. Feng, and G. Xie, "Role of vane configuration on the heat dissipation performance of ventilated brake discs," *Appl. Thermal Eng.*, vol. 136, pp. 118–130, May 2018.

[87] J. Chang, Y. Fan, J. Wu, and B. Zhu, "A yokeless and segmented armature axial flux machine with novel cooling system for in-wheel traction applications," *IEEE Trans. Ind. Electron.*, vol. 68, no. 5, pp. 4131–4140, May 2021.

[88] B. Zhang, Y. Wang, M. Doppelbauer, and M. Gregor, "Mechanical construction and analysis of an axial flux segmented armature torus machine," in *Proc. Int. Conf. Elect. Mach. (ICEM)*, Berlin, Germany, Sep. 2014, pp. 1293–1299.

[89] L. Veg and J. Laksar, "Comparison of two types of cooling of axial flux permanent magnet machines by CFD simulation," in *Proc. Int. Conf. Electr. Drives Power Electron. (EDPE)*, The High Tatras, Slovakia, Sep. 2019, pp. 303–306.

[90] F. Marcolini, G. D. Donato, and F. Caricchi, "Direct oil cooling of end-windings in torus-type axial-flux permanent-magnet machines," in *Proc. IEEE Energy Convers. Congr. Expo. (ECCE)*, Baltimore, MD, USA, Sep. 2019, pp. 5645–5651.

[91] W. Le, M. Lin, L. Jia, and S. Wang, "A cooling enhanced method for axial flux permanent magnet synchronous machine," in *Proc. IEEE Int. Conf. Appl. Supercond. Electromagn. Devices (ASEMD)*, Tianjin, China, Oct. 2020, pp. 1–2.

[92] M. Lampérth, A. Malloy, A. Mlot, and M. Cordner, "Assessment of axial flux motor technology for hybrid powertrain integration," *World Electr. Vehicle J.*, vol. 7, no. 2, pp. 187–194, Jun. 2015.

[93] E. Odvrka, M. Shanel, N. L. Brown, S. Narayanan, C. Ondruek, and A. Mebarki, "Thermal modelling of water-cooled axial-flux permanent magnet machine," in *Proc. 5th IET Int. Conf. Power Electron., Mach. Drives (PEMD)*, Brighton, U.K., 2010, pp. 1–5.

[94] K. M. Rahman, N. R. Patel, T. G. Ward, J. M. Nagashima, F. Caricchi, and F. Crescimbini, "Application of direct-drive wheel motor for fuel cell electric and hybrid electric vehicle propulsion system," *IEEE Trans. Ind. Appl.*, vol. 42, no. 5, pp. 1185–1192, Sep. 2006.

[95] H. Qi, L. Ling, and Z. Liwei, "Design and research of axial flux permanent magnet motor for electric vehicle," in *Proc. IEEE 3rd Int. Electr. Energy Conf. (CIEEC)*, Beijing, China, Sep. 2019, pp. 1918–1923.

[96] W. Liu, Y. Dai, J. Zhao, and X. Wang, "Thermal analysis and cooling structure design of axial flux permanent magnet synchronous motor for electrical vehicle," in *Proc. 22nd Int. Conf. Electr. Mach. Syst. (ICEMS)*, Harbin, China, Aug. 2019, pp. 1–6.

[97] J. Lai, J. Li, and T. Xiao, "Design of a compact axial flux permanent magnet machine for hybrid electric vehicle," *IEEE Trans. Ind. Electron.*, vol. 68, no. 8, pp. 6630–6639, Aug. 2021.

[98] B. Zhang, T. Seidler, R. Dierken, and M. Doppelbauer, "Development of a yokeless and segmented armature axial flux machine," *IEEE Trans. Ind. Electron.*, vol. 63, no. 4, pp. 2062–2071, Apr. 2016.

[99] A. Di Gerlando, G. Foglia, and C. Ricca, "Analytical design of a high torque density in-wheel YASA AFPM motor," in *Proc. Int. Conf. Elect. Mach. (ICEM)*, Gothenburg, Sweden, Aug. 2020, pp. 402–408.

[100] S. Jones-Jackson et al., "Design and analysis of stator cooling channels for an axial-flux permanent magnet machine," in *Proc. IEEE Transp. Electrific. Conf. Expo (ITEC)*, Chicago, IL, USA, Jun. 2021, pp. 272–277.

[101] J. Li, Y. Lu, Y.-H. Cho, and R. Qu, "Design, analysis, and prototyping of a water-cooled axial-flux permanent-magnet machine for large-power direct-driven applications," *IEEE Trans. Ind. Appl.*, vol. 55, no. 4, pp. 3555–3565, Jul. 2019.

[102] A. H. Mohamed, H. Vansompel, and P. Sergeant, "An integrated modular motor drive with shared cooling for axial flux motor drives," *IEEE Trans. Ind. Electron.*, vol. 68, no. 11, pp. 10467–10476, Nov. 2021.

[103] A. H. R. Mohamed, H. Vansompel, and P. Sergeant, "Power density boosting techniques for reconfigurable integrated modular motor drives," *IEEE Trans. Energy Convers.*, vol. 37, no. 3, pp. 1634–1643, Sep. 2022.

[104] R. Camilleri, T. Woolmer, A. Court, and M. D. McCulloch, "Investigation into the temperature profile of a liquid cooled YASA AFPM machine," in *Proc. IET Conf. Publications*, 2012, vol. 2012, no. 592, pp. 1–8.

[105] Z. Zhang, W. Geng, Y. Liu, and C. Wang, "Feasibility of a new ironless-stator axial flux permanent magnet machine for aircraft electric propulsion application," *CES Trans. Electr. Mach. Syst.*, vol. 3, no. 1, pp. 30–38, Mar. 2019.

[106] G. Weiwei, Z. Zhuoran, and L. Qiang, "High torque density fractional-slot concentrated-winding axial-flux permanent-magnet machine with modular SMC stator," *IEEE Trans. Ind. Appl.*, vol. 56, no. 4, pp. 3691–3699, Jul./Aug. 2020.

[107] J. Wanjiku, L. Ge, Z. Zhang, K. Chang, C. Wu, and F. Zhan, "Electromagnetic and direct-cooling analysis of a traction motor," in *Proc. IEEE Energy Convers. Congr. Expo. (ECCE)*, Vancouver, BC, Canada, Oct. 2021, pp. 1461–1467.

[108] R. Camilleri, D. A. Howey, and M. D. McCulloch, "Predicting the temperature and flow distribution in a direct oil-cooled electrical machine with segmented stator," *IEEE Trans. Ind. Electron.*, vol. 63, no. 1, pp. 82–91, Jan. 2016.

[109] P. M. Lindh et al., "Direct liquid cooling in low-power electrical machines: Proof-of-concept," *IEEE Trans. Energy Convers.*, vol. 31, no. 4, pp. 1257–1266, Dec. 2016.

[110] W. Le, M. Lin, L. Jia, and S. Wang, "Design of a novel stator water-cooling system for yokeless and segmented armature axial flux machine," in *Proc. IEEE 4th Student Conf. Electr. Mach. Syst. (SCEMS)*, Huzhou, China, Dec. 2021, pp. 1–4.

[111] W. Tong, R. Tang, Z. An, and Q. Shen, "Water cooling system design and thermal analysis for low speed permanent magnet machines," in *Proc. Int. Conf. Electr. Mach. Syst.*, Beijing, China, Aug. 2011, pp. 1–4.

[112] F. Chai, Y. Bi, and L. Chen, "Thermal investigation and cooling enhancement of axial flux permanent magnet motors for vehicle applications," in *Proc. 22nd Int. Conf. Electr. Mach. Syst. (ICEMS)*, Aug. 2019, pp. 1–5.

[113] Y. Bi, F. Chai, and L. Chen, "The study of cooling enhancement in axial flux permanent magnet motors for electric vehicles," *IEEE Trans. Ind. Appl.*, vol. 57, no. 5, pp. 4831–4839, Sep. 2021.

[114] Q. Huang, L. Luo, and J. Cao, "Investigation of axial flux near-wheel motor for electric vehicle," in *Proc. IEEE 9th Int. Power Electron. Motion Control Conf. (IPEMC-ECCE Asia)*, Nanjung, China, Nov. 2020, pp. 2214–2221.

[115] A. Di Gerlando, G. M. Foglia, M. F. Iacchetti, and R. Perini, "Thermal modeling for the design and check of an axial flux PM motor," in *Proc. Int. Conf. Elect. Mach. (ICEM)*, Berlin, Germany, Sep. 2014, pp. 1441–1447.

[116] J. Li, Y. Lu, Y.-H. Cho, and R. Qu, "Design an analysis of a water-cooled axial flux permanent-magnet machine for large power direct-driven applications," in *Proc. XIII Int. Conf. Electr. Mach. (ICEM)*, Alexandroupoli, Greece, Sep. 2018, pp. 118–124.

[117] H. Vansompel, A. Hemeida, and P. Sergeant, "Stator heat extraction system for axial flux yokeless and segmented armature machines," in *Proc. IEEE Int. Electr. Mach. Drives Conf. (IEMDC)*, May 2017, pp. 1–7.

[118] M. Polikarpova et al., "Hybrid cooling method of axial-flux permanent-magnet machines for vehicle applications," *IEEE Trans. Ind. Electron.*, vol. 62, no. 12, pp. 7382–7390, Dec. 2015.

[119] J. Pyrhönen, P. Lindh, M. Polikarpova, E. Kurvinen, and V. Naumanen, "Heat-transfer improvements in an axial-flux permanent-magnet synchronous machine," *Appl. Therm. Eng.*, vol. 76, pp. 245–251, Feb. 2015.

[120] R. Camilleri and M. D. McCulloch, "Integrating a heat sink into concentrated wound coils to improve the current density of an axial flux, direct liquid cooled electrical machine with segmented stator," *Energies*, vol. 14, no. 12, p. 3619, Jun. 2021.

[121] Q. Wang, X. Li, and Y. Wang, "A HTS stator-excited axial-flux magnetic gear with static seal," *IEEE Trans. Appl. Supercond.*, vol. 31, no. 5, pp. 1–6, Aug. 2021.

[122] A. Reinap, M. Gabassi, M. Alakula, and M. Andersson, "Assessment of cooling integration with direct cooled windings," in *Proc. IEEE Int. Conf. Electr. Syst. Aircr., Railway, Ship Propuls. Road Vehicles Int. Transp. Electrific. Conf. (ESARS-ITEC)*, Nottingham, U.K., Nov. 2018, pp. 1–6.

[123] E. Nitsche and M. Naderer, "Internally cooled hollow wires doubling the power density of electric motors," *ATZelektronik worldwide*, vol. 12, no. 3, pp. 42–47, Jun. 2017.

[124] C. E. Kilbourne and C. H. Holley, "Liquid cooling of turbine-generator armature windings," *Electr. Eng.*, vol. 75, no. 5, pp. 436–441, May 1956.

[125] M. Polikarpova, P. Roytta, J. Alexandrova, S. Semken, J. Nerg, and J. Pyrhonen, "Thermal design and analysis of a direct-water cooled direct drive permanent magnet synchronous generator for high-power wind turbine application," in *Proc. XXth Int. Conf. Electr. Mach.*, Marseille, France, Sep. 2012, pp. 1488–1495.

[126] M. Polikarpova, S. Semken, and J. Pyrhönen, "Reliability analysis of a direct-liquid cooling system of direct drive permanent magnet synchronous generator," in *Proc. Annu. Rel. Maintainability Symp. (RAMS)*, Orland, FL, USA, Jan. 2013, pp. 1–6.

[127] F. Wu and A. M. EL-Refaie, "Additively manufactured hollow conductors with integrated cooling for high specific power electrical machines," in *Proc. Int. Conf. Electr. Mach. (ICEM)*, Gothenburg, Sweden, Aug. 2020, pp. 1497–1503.

[128] C. Wohlers, P. Juris, S. Kabelac, and B. Ponick, "Design and direct liquid cooling of tooth-coil windings," *Electr. Eng.*, vol. 100, no. 4, pp. 2299–2308, Dec. 2018.

[129] (2022). *M2 Series 5 Aluminum Al-Si10-Mg*. [Online]. Available: https://www.ge.com/

[130] (2022). *EOS Aluminium AlSi10Mg Material Data Sheet*. [Online]. Available: https://www.eos.info/

[131] R. Wrobel and R. J. McGlen, "Opportunities and challenges of employing heat-pipes in thermal management of electrical machines," in *Proc. Int. Conf. Elect. Mach. (ICEM)*, Gothenburg, Sweden, Aug. 2020, pp. 961–967.

[132] P. S. Ghahfarokhi et al., "Opportunities and challenges of utilizing additive manufacturing approaches in thermal management of electrical machines," *IEEE Access*, vol. 9, pp. 36368–36381, 2021.

[133] J. C. Corman, R. F. Edgar, M. H. McLaughlin, B. W. Merchant, and R. E. Tompkins, "Heat pipe cooled induction motor," *IEEE Trans. Power App. Syst.*, vol. PAS-93, no. 4, pp. 1069–1075, Jul. 1974.

[134] Y. Sun, S. Zhang, G. Chen, Y. Tang, and F. Liang, "Experimental and numerical investigation on a novel heat pipe based cooling strategy for permanent magnet synchronous motors," *Appl. Thermal Eng.*, vol. 170, Apr. 2020, Art. no. 114970.

[135] A. Lindner and I. Hahn, "Practical evaluation of a passive stator cooling concept without thermal stacking," in *Proc. IEEE Workshop Electr. Mach. Design, Control Diagnosis (WEMDCD)*, Nottingham, U.K., Apr. 2017, pp. 132–139.

[136] M. A. Mueller et al., "Improving the thermal performance of rotary and linear air-cored permanent magnet machines for direct drive wind and wave energy applications," *IEEE Trans. Energy Convers.*, vol. 34, no. 2, pp. 773–781, Jun. 2019.

[137] J. Huang et al., "A hybrid electric vehicle motor cooling system—Design, model, and control," *IEEE Trans. Veh. Technol.*, vol. 68, no. 5, pp. 4467–4478, May 2019.

[138] M. Mochizuki et al., "Hinged heat pipes for cooling notebook PCs," in *Proc. 13th Annu. IEEE Semiconductor Thermal Meas. Manage. Symp.*, Austin, TX, USA, Jan. 1997, pp. 64–72.

[139] F. Wu, A. EL-Refaie, and A. Al-Qarni, "Additively manufactured hollow conductors integrated with heat pipes: Design tradeoffs and hardware demonstration," *IEEE Trans. Ind. Appl.*, vol. 57, no. 4, pp. 3632–3642, Jul. 2021.

[140] P. Szymanski and D. Mikielewicz, "Additive manufacturing as a solution to challenges associated with heat pipe production," *Mater.*, vol. 15, no. 4, pp. 1–17, Feb. 2022.

[141] (2022). *Galden HT 135*. Solvay. [Online]. Available: https://www.solvay.com/en/product/

[142] 1997. *SYLTHERM 800 Heat Transfer Fluid, The Dow Chemical Company*. The Dow Chemical Company. [Online]. Available: https://www.chempoint.com/en-ca/products/dow/syltherm-silicone-thermal-fluids/syltherm-silicone-thermal-fluids/syltherm-800

[143] (2012). *Opticool Fluids Appl. Handling Guide*. Oil Cooled Solutions Worldwide, Tyler, TX, USA. [Online]. Available: https://dsiventures.com/wp-content/uploads/2019/04/Technical-Manual-OPTICOOL.pdf

[144] (2020). *Opteon*. Chemours. [Online]. Available: https://www.opteon.com/en

[145] (2015). *3M Novec Engineered Fluid, 7500, 3M*. [Online]. Available: https://www.3mcanada.ca

[146] (2017). *AmpCool Dielectric Coolants*. Engineered Fluids. [Online]. Available: https://www.engineeredfluids.com/ampcool

[147] (2015). *Therminol Heat Transf. Fluids*. Eastman Chemical Company. [Online]. Available: https://www.therminol.com/heat-transfer-fluids

[148] (2008). *Ethylene Glycol*. The Dow Chemical Company. [Online]. Available: https://www.meglobal.biz/wp-content/uploads/2019/01/Monoethylene-Glycol-MEG-Technical-Product-Brochure-PDF.pdf

[149] S.-S. Hsieh, H.-Y. Leu, and H.-H. Liu, "Spray cooling characteristics of nanofluids for electronic power devices," *Nanosc. Res. Lett.*, vol. 10, no. 1, pp. 1–16, Mar. 2015.

[150] H. Al-Mattarneh and A. Alwadie, "Development of low frequency dielectric cell for water quality application," *Proc. Eng.*, vol. 148, pp. 687–693, Jan. 2016. [Online]. Available: https://www.sciencedirect.com/science/article/pii/S1877705816310219

[151] C. Rhebergen, B. Bilgin, A. Emadi, E. Rowan, and J. Lo, "Enhancement of electric motor thermal management through axial cooling methods: A materials approach," in *Proc. IEEE Energy Convers. Congr. Expo. (ECCE)*, Montreal, QC, Canada, Sep. 2015, pp. 5682–5688.

[152] E. E. Shin, "Improved potting of litz wires for high power density electric motor," in *Proc. AIAA Propuls. Energy Forum*, Denver, CO, USA, Aug. 2021, pp. 1–11.

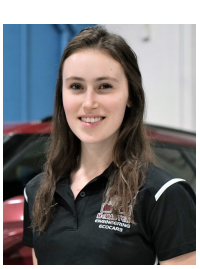

Colleen Jenkins (Student Member, IEEE) received the B.S. and M.S. degrees in mechanical engineering from McMaster University, Hamilton, ON, Canada, in 2020 and 2022, respectively.

During her master's degree, she was the Propulsion Integration Lead of the McMaster Engineering EcoCAR Team, McMaster University, working on hybrid powertrain design and integration. She joined Tesla, Palo Alto, CA, USA, in 2022, where she works on the mechanical design of power electronics. Her research interests include thermal management design and modeling for electric machines.

Samantha Jones-Jackson (Graduate Student Member, IEEE) received the B.S. degree in mechanical engineering from Michigan State University, East Lansing, MI, USA, in 2018. She is currently pursuing the Ph.D. degree in mechanical engineering with McMaster University, Hamilton, ON, Canada.

Her industrial experience focused on automotive applications. During her undergraduate degree, she worked at Delphi, Kokomo, IN, USA, and McLaren, Livonia, MI, USA, as a Mechanical Engineer. Her research interests include thermal management techniques in power electronic modules and electric machines.

Islam Zaher (Student Member, IEEE) received the B.S. degree in mechanical engineering from Ain Shams University, Cairo, Egypt, in 2016, and the M.S. degree in mechanical engineering from McMaster University, Hamilton, ON, Canada, in 2022, where he is currently pursuing the Ph.D. degree in mechanical engineering.

He worked as a Mechanical Design Engineer at the Shaker Consultancy Group, Cairo, from 2018 to 2019. His research interests include the design and simulation of thermal management and turbomachinery systems in electric machines.

Giorgio Pietrini (Member, IEEE) received the B.Sc. and M.Sc. degrees and the Ph.D. degree in information technology from the Department of Information Engineering, University of Parma, Parma, Italy, in 2009, 2014, and March 2019, respectively.

In May 2019, he joined the McMaster Automotive Resource Centre (MARC), McMaster University, Hamilton, ON, Canada, as a Post-Doctoral Fellow. His main research interests include electrical machine design and modeling with special regard to permanent magnet synchronous motors for high-performance automotive traction and aerospace applications.

Romina Rodriguez (Member, IEEE) received the B.S. and M.S. degrees in mechanical engineering from the University of California at Berkeley, Berkeley, CA, USA, in 2010 and 2012, respectively, and the Ph.D. degree in mechanical engineering from McMaster University, Hamilton, ON, Canada, in 2019.

She was a Mechanical Engineer with the Thermal Design an Analysis Group, Northrop Grumman, Los Angeles, CA, USA, from 2012 to 2014. After completing a postdoctoral position at McMaster University in thermal management of power electronics and electric machines, she joined Tesla, San Francisco, CA, USA, in 2021. Currently, she works on the optimization and controls of electrified powertrains.

James Cotton (Senior Member, IEEE) is currently a Professor with the Department of Mechanical Engineering, McMaster University, Hamilton, ON, Canada, where he is also the Co-Director of the McMaster Institute for Energy Studies. His innovation-driven research focuses on developing, modeling, and experimentally validating technologies for automotive thermal management systems, advanced energy harvesting, thermal storage, and integrated community energy systems.

Ali Emadi (Fellow, IEEE) received the B.S. and M.S. degrees (Hons.) in electrical engineering from the Sharif University of Technology, Tehran, Iran, in 1995 and 1997, respectively, and the Ph.D. degree in electrical engineering from Texas A&M University, College Station, TX, USA, in 2000.

Before joining McMaster University, Hamilton, ON, Canada, he was the Harris Perlstein Endowed Chair Professor of engineering and the Director of the Electric Power and Power Electronics Center and Grainger Laboratories, Illinois Institute of Technology (Illinois Tech), Chicago, IL, USA, where he established research and teaching facilities, as well as courses in power electronics, motor drives, and vehicular power systems. He was the Founder, the Chairperson, and the President of Hybrid Electric Vehicle Technologies, Inc. (HEVT)—a university spin-off company of Illinois Tech. He is currently the Canada Excellence Research Chair Laureate with McMaster University. He is also the holder of the NSERC/FCA Industrial Research Chair in Electrified Powertrains and the Tier I Canada Research Chair in Transportation Electrification and Smart Mobility. He is also the President and the Chief Executive Officer of Enedym Inc. and Menlolab Inc.—two McMaster University spin-off companies. He is the principal author/coauthor of over 500 journal articles and conference papers, and several books, including *Vehicular Electric Power Systems* (2003), *Energy Efficient Electric Motors* (2004), *Uninterruptible Power Supplies and Active Filters* (2004), *Modern Electric, Hybrid Electric, and Fuel Cell Vehicles* (second edition, 2009), and *Integrated Power Electronic Converters and Digital Control* (2009). He is also the editor of *Handbook of Automotive Power Electronics and Motor Drives* (2005) and *Advanced Electric Drive Vehicles* (2014). He is a coeditor of the *Switched Reluctance Motor Drives* (2018).

Dr. Emadi was the Inaugural General Chair of the 2012 IEEE Transportation Electrification Conference and Expo (ITEC) and has chaired several IEEE and SAE conferences in the areas of vehicle power and propulsion. He was the Founding Editor-in-Chief of the IEEE TRANSACTIONS ON TRANSPORTATION ELECTRIFICATION from 2014 to 2020.